

RESEARCH ARTICLE SUMMARY

TRANSPOSON

Structural mechanism of LINE-1 target-primed reverse transcription

George E. Ghanim*, Hongmiao Hu, Jerome Boulanger, Thi Hoang Duong Nguyen*

INTRODUCTION: Long interspersed element-1 (LINE-1) retrotransposons are the most abundant and the only active autonomous transposable element in humans, accounting for ~17% of the human genome. LINE-1 activity can have profound effects on genomic integrity and has been strongly linked to cancers and various other diseases. The propagation of LINE-1 occurs through a mechanism called target-primed reverse transcription (TPRT). During TPRT, the open reading frame 2 protein (ORF2p), encoded by LINE-1, cleaves the target DNA and reverse transcribes LINE-1 messenger RNA (mRNA) into a new genomic location. To complete the insertion, a second cleavage on the opposite DNA strand and DNA synthesis of this second strand are necessary. The staggered nature of the two cleavages leads to the duplication of the target sequence at both ends of the insertion, a feature known as target site duplication (TSD). However, how ORF2p reorganizes the target DNA for reverse transcription, whether ORF2p nicks both target DNA strands, the factors influencing the variable

length of the TSDs, and the involvement of host factors in this process remain largely unknown.

RATIONALE: In this study, we aimed to dissect the molecular mechanisms underlying LINE-1 retrotransposition. We sought to understand how ORF2p handles nucleic acids during TPRT by biochemically and structurally capturing a LINE-1 TPRT complex, which includes ORF2p, a substrate RNA, and an authentic target DNA derived from the human factor VIII gene. Using AlphaFold3 structure prediction, we also explored potential interactions with host factors to elucidate their roles in LINE-1 retrotransposition.

RESULTS: We biochemically stalled ORF2p during TPRT by bypassing the first nicking step and resolved four structures of the TPRT complex using cryo-electron microscopy (cryo-EM). Our structures show that ORF2p bends and unwinds the target DNA, inserting the nicked 3' end into its active site to prime reverse transcription. We observe that the

second DNA strand is also nicked in the TPRT structures. Biochemical experiments confirmed that the endonuclease domain of ORF2p is responsible for second-strand nicking, either before or concurrently with the reverse transcription of the first strand. Structural analysis suggests that the flexibility of the endonuclease domain, along with target DNA unwinding, may contribute to the variability in TSD length.

Notably, the identified nicking sites are close to but do not coincide with the putative nicking site from the patient-derived target DNA sequence. This discrepancy could be attributed to interactions between the LINE-1 ribonucleoprotein (RNP) and other cellular factors. AlphaFold3 predictions identify previously unknown interaction sites on ORF2p for proliferating cell nuclear antigen (PCNA) and cytoplasmic poly(A)-binding protein 1 (PABPC1). These binding sites are highly conserved and are critical for retrotransposition. The predicted binding site for PCNA aligns with the position of target DNA in our cryo-EM structure. The predicted interaction with PABPC1 may explain a phenomenon known as cis-preference, in which ORF2p preferentially associates with its encoding mRNA.

Together with structure predictions, our structure and associated experiments allow us to expand on the model of LINE-1 retrotransposition. First, cotranslational interaction between ORF2p and PABPC1 may facilitate ORF2p association with its own mRNA. Upon RNP formation and nuclear import, LINE-1 RNP may be recruited to a target DNA by interaction with PCNA. ORF2p cleaves the first strand, remodels the target DNA, and cleaves the second strand before or during first-strand synthesis. Once the first strand is copied, ORF2p synthesizes the second strand by priming from the nicked second strand, resulting in a new LINE-1 insertion. In this model, premature initiation of second-strand synthesis would result in 5' truncated insertions.

CONCLUSION: We present the structure of a human LINE-1 TPRT complex, providing insights into the extensive remodeling of the target DNA by ORF2p and clarifying the mechanism of second-strand nicking. We describe previously unidentified PCNA and PABPC1 binding sites on ORF2p, highlighting their potential involvement in LINE-1 retrotransposition. Together, our findings propose a revised model for LINE-1 retrotransposition, detailing an updated sequence of events for TPRT. ■

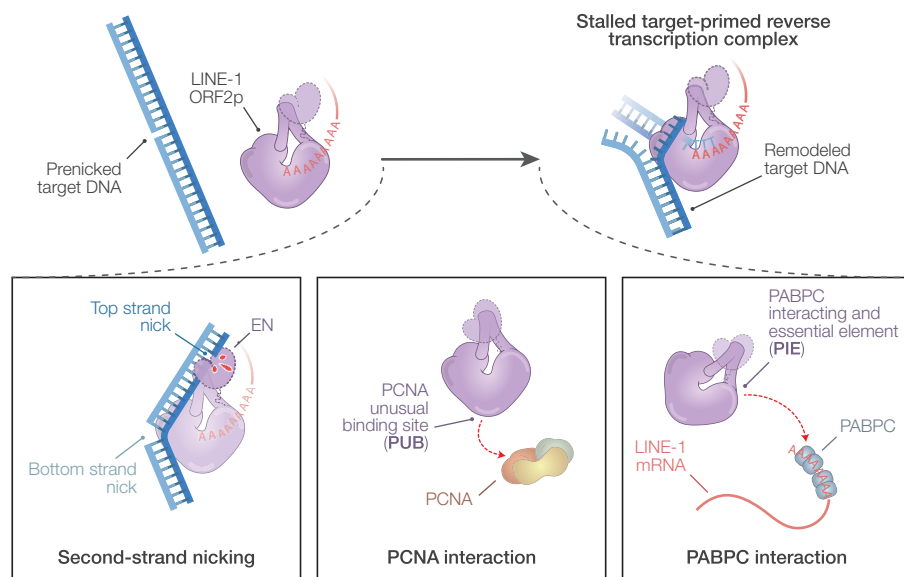
The list of author affiliations is available in the full article online.

*Corresponding author. Email: gghanim@princeton.edu

(G.E.G.); knguyen@mrc-lmb.cam.ac.uk (T.H.D.N.)

Cite this article as G. E. Ghanim *et al.*, *Science* 388, eads8412 (2025). DOI: 10.1126/science.ads8412

S READ THE FULL ARTICLE AT
<https://doi.org/10.1126/science.ads8412>



Structural insights from the LINE-1 ORF2p TPRT complex. ORF2p remodels the target DNA in the LINE-1 TPRT complex and nicks the second strand before or with reverse transcription of the first strand. Structure predictions suggest roles for two LINE-1-associated factors, PCNA and PABPC, in the retrotransposition process. EN, endonuclease.

RESEARCH ARTICLE

TRANSPOSON

Structural mechanism of LINE-1 target-primed reverse transcription

George E. Ghanim*†, Hongmiao Hu, Jerome Boulanger, Thi Hoang Duong Nguyen*

Long interspersed element-1 (LINE-1) retrotransposons are the only active autonomous transposable elements in humans. They propagate by reverse transcribing their messenger RNA into new genomic locations by a process called target-primed reverse transcription (TPRT). In this work, we present four cryo-electron microscopy structures of the human LINE-1 TPRT complex, revealing the conformational dynamics of open reading frame 2 protein (ORF2p) and its extensive remodeling of the target DNA for TPRT initiation. We observe nicking of the DNA second strand during reverse transcription of the first strand. Structure prediction identifies high-confidence binding sites for LINE-1-associated factors—namely proliferating cell nuclear antigen (PCNA) and cytoplasmic poly(A)-binding protein 1 (PABPC1)—on ORF2p. Together with our structural data, this suggests a mechanism by which these factors regulate retrotransposition and supports a model for TPRT that accounts for retrotransposition outcomes observed in cells.

Retrotransposons are genetic sequences that can move through a host genome by means of an RNA intermediate (1). Long interspersed element-1 (LINE-1) and *Alu* elements are the most abundant retrotransposable elements within the human genome, constituting nearly 30% of the genome by sequence (2). Although most are inactive, a small subset of LINE-1 and *Alu* elements can still mobilize (3–6). Consequently, this mobility can lead to substantial genetic mutations. Retrotransposition results in numerous genetic diseases (7), is thought to drive oncogenic rearrangements in certain cancers (8), and is linked to age-related inflammation (9). Beyond their effect on health, there has been renewed interest in developing retrotransposons and other transposable elements for biotechnological applications (10–15).

LINE-1 retrotransposition is performed by a ribonucleoprotein (RNP) complex composed of the LINE-1 mRNA bound by two encoded proteins, open reading frame 1 protein (ORF1p) and ORF2p (Fig. 1, A and B) (16, 17). ORF1p acts as a cytoplasmic RNA chaperone (18), whereas ORF2p has both endonuclease (EN) (19) and reverse transcriptase (RT) activities (20). New genomic copies of LINE-1 are generated through a process called target-primed reverse transcription (TPRT) (21). During TPRT, ORF2p nicks the first “bottom” strand of a 5′-TT|AAAA-3′ target DNA sequence, exposing a 3′ end that primes reverse transcription of the LINE-1 mRNA (Fig. 1B) (19, 22). The subsequent

nicking of the second “top” DNA strand, followed by second-strand synthesis, results in a new genomic copy of the retrotransposon. The staggered nicking of the top strand relative to the bottom strand gives rise to characteristic 7- to 20-nucleotide (nt) target site duplications (TSDs) flanking the retrotransposon (23, 24).

Recent landmark structures of ORF2p assembled on short RNA-DNA duplexes provide insights into how the first strand of cDNA synthesis is extended (25, 26). However, these studies did not capture the TPRT complex because they had used only single-stranded DNA substrates rather than an authentic double-stranded target DNA. As a result, it remains unclear how ORF2p handles the LINE-1 mRNA and target DNA during TPRT. Additionally, insights into top strand nicking by ORF2p cannot be inferred from these structures (25, 26). Whether or when the top strand is nicked by the ORF2p EN domain and how TSDs of varying lengths arise remain unknown.

A target DNA intermediate stimulates TPRT

To understand the biochemical requirements for TPRT, we first purified ORF2p from baculovirus-infected insect cells (fig. S1A) and tested its TPRT activity in vitro using an RNA substrate and a fluorescently labeled prenicked target DNA (fig. S1B). Although purified ORF2p displayed TPRT activity, our initial preparations were ~99.9% inactive and would not suffice for structural characterizations. Therefore, we used an activity-based purification approach to isolate fractions of ORF2p with high specific TPRT activity (see Materials and methods) (fig. S1C).

To identify an ideal RNA for structural studies, we performed TPRT assays with either

an *Alu* RNA or a 30-nt poly(A) (pA₃₀) RNA substrate (fig. S1B). TPRT activity and low levels of template jumping were only observed in the presence of deoxynucleotide triphosphates (dNTPs) and an *Alu* RNA substrate (Fig. 1C). However, increasing concentrations of *Alu* RNA inhibited TPRT activity (Fig. 1C, lanes 4 to 6). Unlike the *Alu* RNA, the pA₃₀ RNA resulted in higher overall activity, and increasing concentrations did not inhibit but rather stimulated TPRT activity (Fig. 1D). The pA₃₀ substrate was also highly efficient for template jumping, producing large TPRT products (Fig. 1D). Given the stimulation, the pA₃₀ RNA was used in subsequent assays and in TPRT complex formation.

We next explored the influence of the target DNA architecture on TPRT activity. The target DNA for our assays was derived from the human factor VIII gene, at the locus where de novo LINE-1 insertions were first identified (27), and was idealized to introduce a stronger EN motif at the insertion site (fig. S1B). Additionally, the target DNA was prenicked on the bottom strand of the TTAAAA insertion consensus. This substrate mimics an intermediate of retrotransposition after bottom strand nicking by the EN domain of ORF2p (fig. S1B). Idealization of the target DNA subtly stimulated TPRT activity (fig. S1D, lanes 4 and 6). As suggested by previous studies, a prenicked target DNA greatly stimulated TPRT activity (Fig. 1E, lane 4) (28). By contrast, the levels of TPRT activity on unnicked DNA substrates were nearly imperceptible under the reaction conditions tested (Fig. 1E, lane 2). Mutating the TTAAAA consensus sequence to CCGGCG in the nicked substrate abolished the stimulation (Fig. 1E, lane 6). This demonstrates that a nicked DNA substrate alone is insufficient for TPRT and implies some sequence specificity in the target site of ORF2p. This is consistent with a previously proposed model where complementarity between target DNA primer and RNA template influences the efficiency of reverse transcription (29, 30).

We further evaluated the TPRT activity of our purified ORF2p on alternative target DNA designs, including substrates with a 3′ overhang used in previous studies (26). Although these substrates supported bottom strand nicking and TPRT activity (fig. S1E, lanes 2 and 4), this activity was abolished if the substrates were made fully double stranded (fig. S1F, lanes 2 and 6). TPRT activity was restored when the double-stranded substrates were prenicked on the bottom strand (fig. S1F, lanes 4 and 8). It remains unclear whether substrates with a 3′ overhang bypass the physiological requirements for retrotransposition or represent authentic physiological targets. Similar observations have been reported with other nucleoprotein reactions, where alternative

MRC Laboratory of Molecular Biology, Cambridge, UK.

*Corresponding author. Email: gghanim@princeton.edu (G.E.G.); knguyen@mrc-lmb.cam.ac.uk (T.H.D.N.)

†Present address: Department of Molecular Biology, Princeton University, Princeton, NJ, USA.

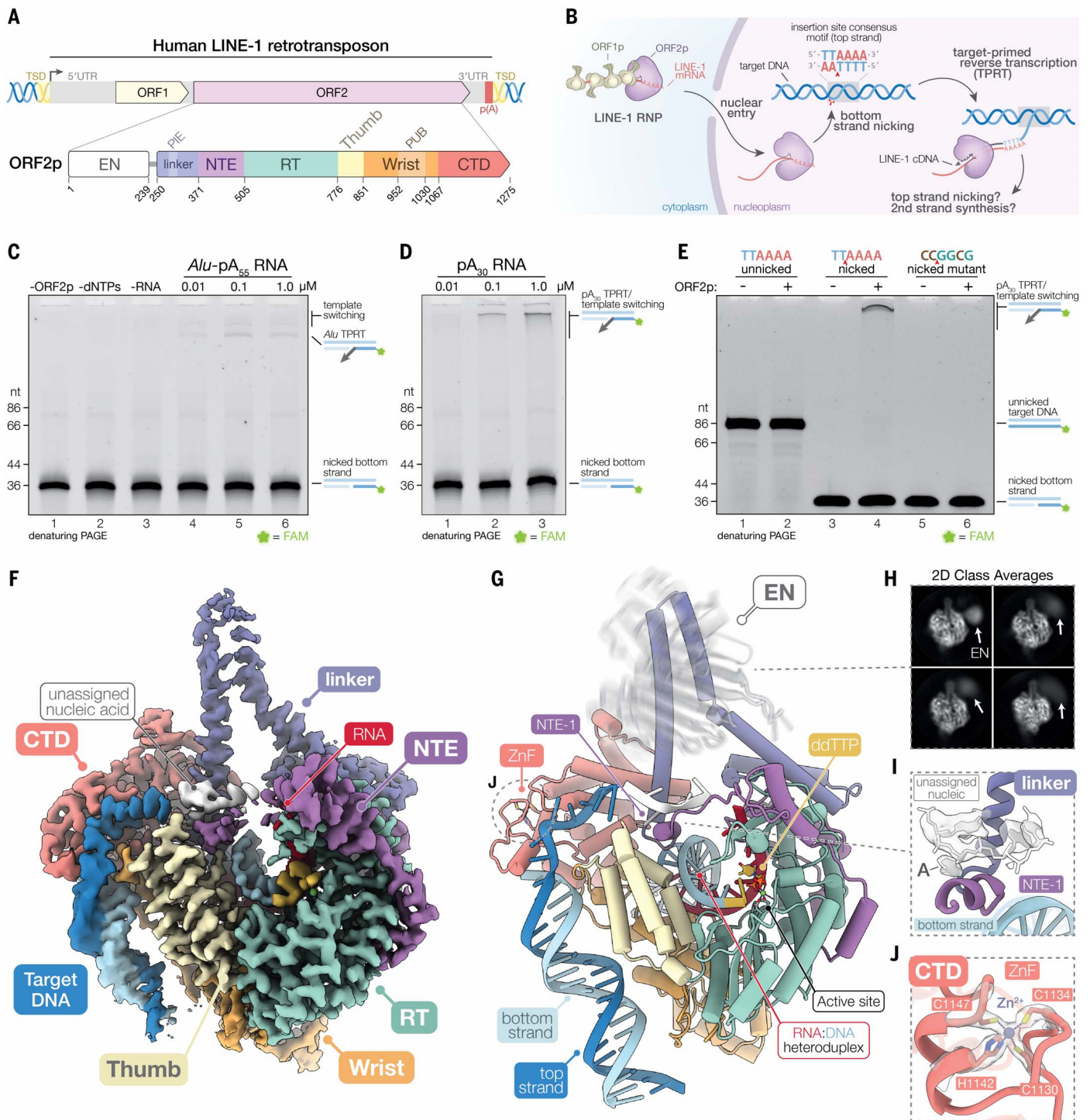


Fig. 1. Cryo-EM structure of the LINE-1 TPRT complex. (A) Organization of the human LINE-1 retrotransposon and domains of ORF2p. linker, EN linker; UTR, untranslated region. (B) Schematic of LINE-1 retrotransposition. (C) Denaturing gel showing TPRT activity with an *Alu* RNA template. (D) Denaturing gel showing TPRT activity with a pA₃₀ RNA. (E) Denaturing gel showing the effects of unnicked, prenicked, or mutated prenicked target DNA substrate on TPRT activity. (F) Composite 2.3-Å cryo-EM reconstruction of the LINE-1 TPRT complex. Linker and target DNA densities were blurred to

highlight flexible features. (G) Atomic model of the LINE-1 TPRT complex. (H) 2D class averages showing flexibility of the EN domain. (I) Unassigned nucleic acid contacts the NTE. Cryo-EM density is shown as a transparent surface and blurred to highlight flexible features. (J) CTD ZnF. Cryo-EM density is shown as a transparent surface. Single-letter abbreviations for the amino acid residues are as follows: A, Ala; C, Cys; D, Asp; E, Glu; F, Phe; G, Gly; H, His; I, Ile; K, Lys; L, Leu; M, Met; N, Asn; P, Pro; Q, Gln; R, Arg; S, Ser; T, Thr; V, Val; W, Trp; and Y, Tyr.

DNA substrates (e.g., prenicked, short flanking DNA or noncomplementary flanking DNA) bypass physiological requirements (31, 32). Our observations highlight the importance of substrate design in understanding the mechanistic requirements of retrotransposition.

Cryo-electron microscopy (cryo-EM) structure and architecture of ORF2p in the TPRT complex

To understand the molecular basis underlying TPRT, we implemented a strategy to assemble and purify active ORF2p with pA₃₀ RNA, the prenicked target DNA, and the chain terminator 2',3'-dideoxythymidine triphosphate (ddTTP) for structure determination by cryo-EM (fig. S2). We obtained a 2.3-Å-resolution reconstruction of the human ORF2p TPRT complex stalled after initiation (Fig. 1F, figs. S3 to S5, and table S1).

The domains of ORF2p adopt a basketlike shape that accommodates the RNA-DNA duplex in the RT active site (Fig. 1, F and G), as observed in the previous structures (supplementary text) (25, 26). ORF2p can be divided into six structural domains: an N-terminal EN domain, an EN linker domain (linker) (26), an N-terminal extension (NTE) domain (26), an RT domain and thumb subdomain, the wrist domain (25), and the C-terminal segment domain (CTD) (33) (Fig. 1, A, F, and G).

The EN domain belongs to a larger class of apurinic/aprimidinic endonuclease-like domains and connects to the rest of ORF2p by a short flexible linker but was poorly resolved in our consensus reconstruction owing to its apparent flexibility (Fig. 1H). Following the EN domain are the linker domain and NTE domain. The NTE domain has been implicated in template switching (34), whereas the linker domain features two long helices that form the so-called “handle” of the basketlike architecture (Fig. 1, F and G). Together, the linker and NTE regions (residues 240 to 440) are also collectively referred to as the tower domain (25).

A region of the NTE domain, called NTE-1 (residues 362 to 381) (Fig. 1G, NTE-1), resembles that in the related *Bombyx mori* R2 encoded ORF (*BmR2*) (35) and alpha helix-1 (residues 953 to 958) of the C-terminal extension domain of the human telomerase reverse transcriptase (TERT) (fig. S6, A and B) (36). Analogous to the *BmR2* NTE-1 contacts with its target DNA and template RNA, ORF2p NTE-1 contacts both the target DNA and another nucleic acid strand (Fig. 1I, unassigned nucleic acid, and fig. S6A). The identity of this nucleic acid strand remains unclear because it was disconnected from the surrounding nucleic acid densities. We noted that this ambiguous density resembled adenosine bases and adenosine base-specific interactions, which suggests that it may be part of the pA₃₀ RNA.

The RT and thumb lie at the core of basket and together adopt the right-hand fold characteristic of DNA polymerases and RTs (Fig. 1, F and G) (37). The mechanism for DNA synthesis is shared among RTs and DNA polymerases and involves successive conformational changes to their active site at each round of nucleotide addition (37). After the correct base-pairing with the incoming dNTP is formed, the fingers subdomain and RT-specific motif D rotate toward the RT active site and close around the dNTP (37).

During cryo-EM image processing, we observed lower local resolution estimates near the RT active site, which suggests the presence of alternative conformations. Focused classification revealed two configurations of the RT active site, which we refer to as the open fingers state and closed fingers state (figs. S3, S7, and S8 and movie S1). In the open fingers state, the fingers subdomain and motif D rotate outward from the active site, with weak density observed at the fingertips and for the base of the incoming dNTP (fig. S8A). Conversely, in the closed state, the fingers and motif D are rotated inward and close around the incoming dNTP (fig. S8B). This closed conformation allows numerous contacts to form between the dNTP and the RT (fig. S8B). Observing these states in our dataset highlights the plasticity of the RT active site, which is necessary to achieve the processivity observed during DNA synthesis.

The wrist and CTD follow the RT domain and lie at the C terminus of ORF2p. The CTD harbors the essential cysteine-rich motif (6, 33), which adopts a C₂HC zinc finger (ZnF) fold (Fig. 1, G and J). We find that the CTD melts and interacts extensively with the target DNA, rather than with the substrate RNA as previously suggested (Fig. 1, F and G) (26, 38).

ORF2p extensively remodels the target DNA to initiate TPRT

Our structure reveals the full engagement of ORF2p with the target DNA and the pA₃₀ template RNA (Fig. 2A). ORF2p binding creates a sharp bend in the target DNA and roughly breaks it into two parts. We refer to these parts as the first primer region and the second primer region (Fig. 2, A and B). The first primer region corresponds to the target DNA with the nicked bottom strand that primes first-strand cDNA synthesis of the template RNA (Fig. 2, B and C). Accordingly, this region harbors the template:primer heteroduplex formed by the pA₃₀ template RNA and the nicked bottom strand primer (Fig. 2, C and D). Similar to previous structures (25, 26), the RT domain positions the heteroduplex within the RT active site, with varying contributions from the other domains of ORF2p (Fig. 2D).

The second primer region, which has not been captured in previous structures, includes

the region of the target DNA with the top strand anticipated to prime second-strand synthesis (Fig. 2, B and E). It is anchored at one end by a highly positive surface formed by the thumb, wrist, and CTD domains (Fig. 2E).

We routinely observed varying lengths of the second primer target DNA region in different three-dimensional (3D) cryo-EM classes (fig. S9, A and B, and movie S2). Close inspection of the consensus cryo-EM map showed that the CTD unzipped the target DNA duplex by wedging the ZnF between the top and bottom strands. Two isoleucine residues extend from the ZnF helix to stack against the bases of the target DNA duplex (Fig. 2F). The melted top strand bends through a positively charged cleft formed by the CTD and wrist domain and then binds along the CTD toward the RT active site (Fig. 2H). In an almost ruler-like mechanism, the last 5 nt are sandwiched between Asn¹²⁰⁹ and Pro⁸⁰³ from the CTD and thumb domain, respectively (Fig. 2H). These nucleotides adopt a nearly ideal B-form DNA geometry (fig. S9C). The phosphate backbone is buried into the surface of the CTD, and the base edges are exposed to the solvent.

A similar unzipping of the target DNA by a ZnF has been observed in the TPRT structure of *BmR2* (Fig. 2G) (35). Although the role of the ZnF in unzipping the target DNA to initiate TPRT may be evolutionarily conserved, ORF2p may use a mechanism that is distinct from that of *BmR2* for target DNA handling. Moreover, the extent of DNA remodeling differs from the target DNA bending observed in many DNA transposase and retroviral integrase systems (39) but is more akin to the nucleic acid rearrangements performed by CRISPR-Cas proteins (40).

The top strand is nicked by the EN domain

The prevailing model for LINE-1 insertion consists of two steps: first-strand synthesis and second-strand synthesis (21). Under this model, ORF2p first nicks the bottom strand of the target DNA and then uses this nicked bottom strand to prime first-strand synthesis of the RNA template (28). It is thought that the top strand is nicked and primes second-strand synthesis after the first strand is synthesized. Our TPRT complex was stalled immediately after initiation and before completion of first-strand synthesis. We had, therefore, expected to see that only the bottom strand was nicked and that there was an unnicked top strand bridging the first and second primer regions of the target DNA. However, our cryo-EM map showed that the top strand appeared to be nicked.

To validate this observation, we performed TPRT assays using a target DNA substrate doubly labeled with FAM and Cy5 fluorophores on the top and bottom strands, respectively. This design allows us to simultaneously track

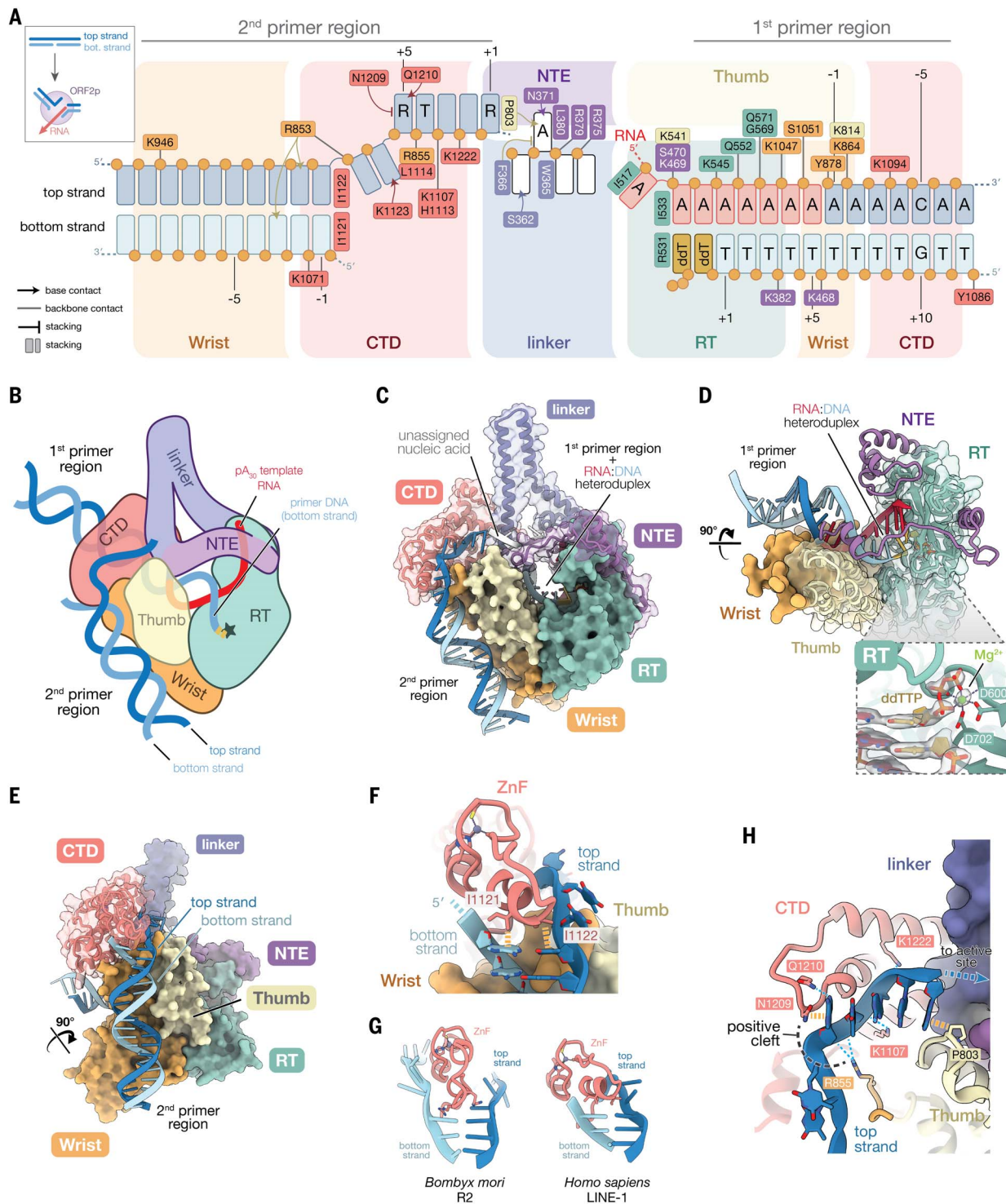


Fig. 2. The target DNA is unzipped and broken across the domains of ORF2p. (A) Schematic of ORF2p interactions with the target DNA. Top and bottom strands are numbered relative to their respective cleavage sites. (Inset) Simplified schematic of target DNA remodeling accompanying TPRT complex formation. (B) Cartoon of the TPRT complex. Green star indicates RT active site. (C) Structure highlighting interactions with the two target DNA regions. (D) Structure surrounding

the first primer region of the target DNA. (Inset) View of ddTTP in the RT active site; cryo-EM density is shown as a transparent surface. (E) Structure surrounding the second primer region of the target DNA. (F) CTD ZnF unzips the target DNA. Yellow dashed lines indicate stacking interactions. (G) Comparison of target DNA unzipping by *BmR2* ZnF (35). (H) Interactions with the melted top strand and ORF2p. Blue dashed lines indicate hydrogen bonding.

first-strand synthesis, top strand nicking, and second-strand synthesis. A time course of the TPRT assay showed that the top strand is indeed nicked, with cleavage primarily occurring at three positions (Fig. 3A, top). These nicked products accumulated over time (Fig. 3A, top) and tracked with the accumulation of the bottom strand TPRT product (Fig. 3A, bottom). Top strand nicking occurred in cis (fig. S10A), and the cleavage pattern was not affected by the sequence at the RNA 5' end (fig.

S10B). An EN catalytic site mutant, D145A (19, 41), blocked top strand nicking and attenuated bottom strand TPRT products (Fig. 3B, EN-). Taken together, these results indicate that the EN domain nicks the top strand and that top strand nicking does not license reverse transcription of the bottom strand.

We next sought to define the positions of the top strand cleavage sites by Sanger sequencing. Comparison with a DNA sequencing ladder showed that top strand nicking occurs up-

stream of the insertion consensus motif and is staggered +7, +11, and +19 nt relative to the bottom strand nick (Fig. 3C, arrows 3, 2, and 1, respectively, and fig. S10C). Staggered nicking of the top strand leads to the characteristic TSDs that flank new retrotransposon insertions. The spacing observed in our assay is within the reported lengths of in vivo LINE-1 TSD events (23, 24). Furthermore, our TPRT structure would represent a mixture of states of the target DNA owing to the heterogeneity in the cutting sites, together with the ability of ORF2p to unzip the target DNA. This would account for the ambiguity in the densities of the DNA bases in our consensus cryo-EM map (Fig. 2A). We did not observe nicking at the putative top strand cleavage site of patient JH-27, from whom this target DNA sequence was derived (Fig. 3C and fig. S10C) (27). This discrepancy was not caused by idealization of the target DNA because the same cutting sites were observed using a substrate with the native factor VIII sequence (fig. S10D). We also note that only one of the three top strand cleavage sites resembled the EN cleavage consensus motif (Fig. 3C, site 1), although previous studies have suggested that bottom and top strand cleavage events may have different sequence preferences (22). Alternatively, these differences may arise from the lack of host factors that could affect cleavage site choice. Overall, our TPRT structure suggests an updated sequence of events for TPRT, in which top strand nicking occurs with or during first-strand synthesis, and may explain why most LINE-1 insertions are 5' truncated or 5' inverted (42–47).

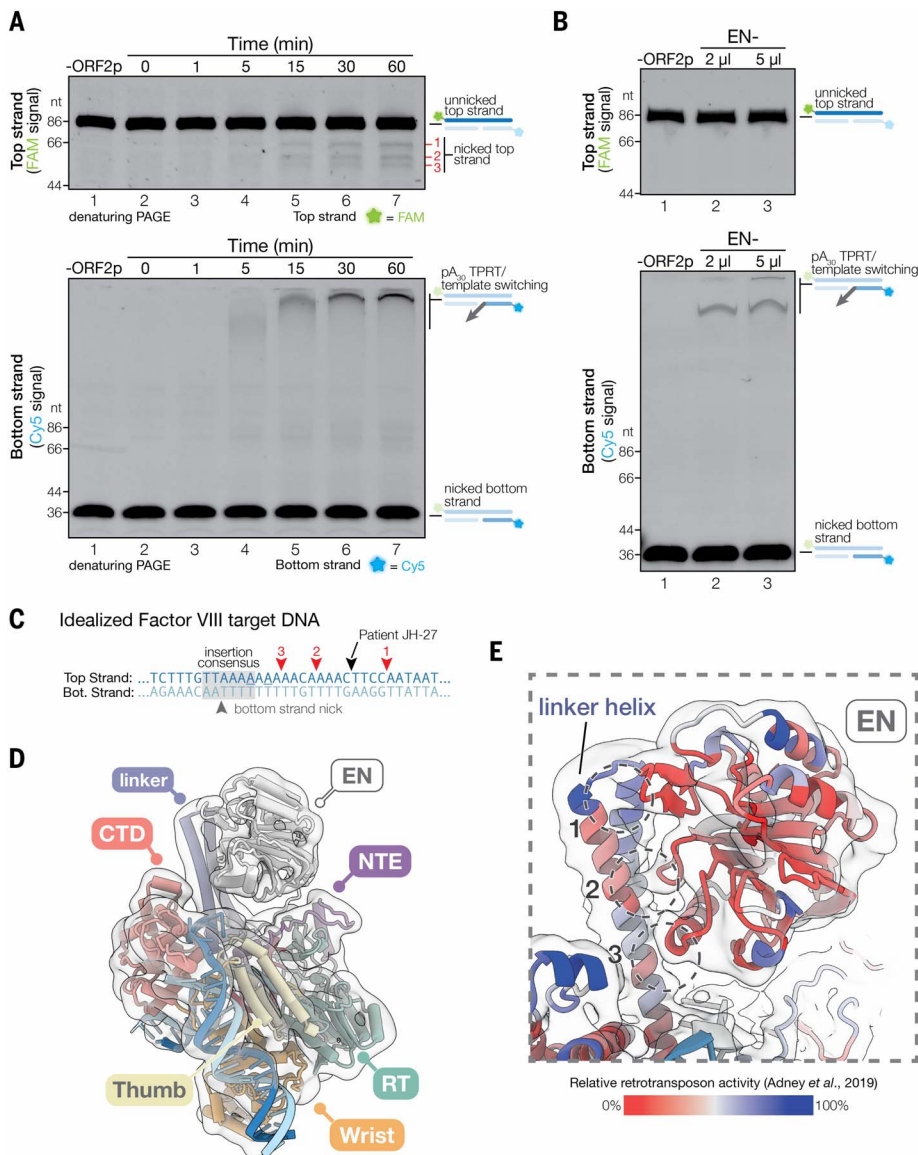


Fig. 3. The top strand is nicked with reverse transcription. (A) Top strand nicking correlates with bottom strand TPRT. Denaturing gel of TPRT assay time course with doubly fluorescently labeled target DNA, visualized by FAM fluorescence to show top strand nicking (top) or by Cy5 fluorescence to show bottom strand TPRT products (bottom). (B) EN- (D145A) mutant blocks top strand nicking and reduces bottom strand TPRT. (C) Schematic of target DNA nicking. Red numbered arrowheads indicate the mapped cleavage sites of the top strand-nicked products in (A). (D) Cryo-EM reconstruction with the EN domain resolved. Atomic model fit into the density is shown. Cryo-EM map was low-pass filtered to 8 Å. (E) Detailed view of EN-linker domain contacts. Retrotransposition efficiencies from alanine scanning substitutions (50) are mapped onto the structure. Cryo-EM map was low-pass filtered to 5 Å.

Conformational plasticity of the EN domain

We observed weak density near the long helices of the linker domain. We investigated whether this corresponded to the EN domain in a more stable configuration, although it was too flexible to resolve in our consensus reconstruction. Through iterative rounds of focused classification and local refinement with Blush regularization (48), we resolved this domain to moderate resolutions (4.0 to 6.5 Å) (Fig. 3D and fig. S11). Docking a crystal structure of the EN domain (49) into the resulting cryo-EM map shows three main contacts with the long helix of the linker domain (Fig. 3E, circles 1, 2, and 3). Alanine scanning substitutions (50) at either the EN or linker contact sites decrease retrotransposition activity of LINE-1, whereas substitutions of the neighboring linker helix do not (Fig. 3E). This suggests that these interactions are important for LINE-1 retrotransposition.

Although the flexibility of the EN domain and the melting of the target DNA were unexpected findings, they may explain the varying TSD lengths flanking new retrotransposon insertions. These TSDs arise from the staggered cleavage of the target DNA top strand relative

to the bottom strand nick and are variable in length but usually <20 nt (23, 24). Modeling a nicked target DNA into our EN-resolved map places the EN domain ~20 nt away from the bottom strand nick (fig. S11G) and may represent the default configuration of the EN domain for top strand nicking. Target DNA unzipping and ORF2p sliding would draw the bottom strand nick toward the EN domain, resulting in TSDs shorter than 20 nt (Fig. 5, step 4). This mechanism, coupled with the flexibility of the EN domain, may allow ORF2p to sample the target DNA for an ideal top strand cleavage site before committing to first-strand synthesis.

Cellular factors facilitate nucleic acid binding

Many of the interactions between ORF2p and the target DNA and template RNA are made through the phosphate backbone and are not sequence specific. This was unexpected because LINE-1 retrotransposition demonstrates at least two nucleic acid specificities: (i) insertion at EN consensus cleavage sites (19, 22, 51) and (ii) reverse transcription of its own mRNA, which requires the poly(A) tract (52). The *in vitro* top strand cleavage sites did not match patient JH-27 (27), contrary to our expectations. Numerous cellular proteins are known to associate with the LINE-1 RNP, and some are essential for retrotransposition (53–58), which raises the possibility that these proteins facilitate the nucleic acid specificity of LINE-1 retrotransposition.

To assess this, we used AlphaFold3 to predict the structures of ORF2p with a nonredundant list of known interactors (data S1) (54, 55, 59). High-confidence interactions with proliferating cell nuclear antigen (PCNA) and cytoplasmic poly(A)-binding protein 1 (PABPC1) stood out among the predicted structures (Fig. 4 and figs. S12 and S13).

PCNA binds a previously unknown site on ORF2p

Human PCNA, also known as the sliding clamp, is a homotrimeric DNA processivity factor and is essential to DNA replication and repair (60). PCNA copurifies with the LINE-1 RNP and was proposed to interact with a canonical PCNA-interacting peptide (PIP) box motif in the NTE domain of ORF2p (residues 407 to 415) (25, 54).

However, AlphaFold3 predicted that PCNA interacts with the wrist domain of ORF2p instead (Fig. 4A and fig. S12, A to C). The predicted ORF2p-PCNA interaction differs substantially from canonical PIP box-PCNA interactions (Fig. 4B, fig. S12D, and supplementary text). In this case, we find that a helix from the ORF2p wrist domain lies along the PCNA hydrophobic pocket, against the interdomain connector loop (IDCL) (Fig. 4B), to bury Trp¹⁰¹¹ and Ile¹⁰¹⁴. Additionally, Asn⁹⁶⁸ from a neighboring loop of the wrist domain extends into the PCNA Q-pocket. This mimics the typical

glutamine-Q-pocket interaction typically observed in canonical PIP box-PCNA interactions (Fig. 4B). We call these regions of the ORF2p wrist domain the PCNA unusual binding (PUB) motif.

Four pieces of evidence support the prediction: (i) The predicted PUB-PCNA interaction places PCNA directly in line with the target DNA in our cryo-EM structure (Fig. 4A). (ii) Trialanine scanning substitutions (50) at residues in the PUB motif severely disrupt retrotransposition (Fig. 4C). (iii) ORF2p W1011A (Trp¹⁰¹¹→Ala) and I1014A PUB mutants are defective in binding to PCNA in ORF2p pull-down experiments (Fig. 4D). (iv) PUB motif residues predicted to interact with PCNA are highly conserved across LINE-1 elements from divergent species (fig. S12E, starred residues).

PABPC1 binds near the template RNA entry channel of ORF2p

PABPC1 belongs to a family of highly abundant cytoplasmic poly(A)-binding proteins, which regulate numerous facets of mRNA biology, including translation initiation, deadenylation, and mRNA decay (61–68). PABPC1 binds RNA through four consecutive RNA-recognition motif (RRM) domains, where RRM1 and RRM2 mainly confer adenosine-binding specificity and affinity (69–72). Previous studies have shown that PABPC1 is a component of the LINE-1 RNP and is required for efficient retrotransposition by promoting cytoplasmic RNP formation (53–55). Yet, it is unclear whether PABPC1 directly interacts with LINE-1 components or whether its association is simply explained by binding to the LINE-1 mRNA poly(A) tail (55).

Our structure predictions show that the RRM1 of PABPC1 directly binds the linker domain of ORF2p (residues 272 to 297) through numerous side chain-backbone and side chain-side chain interactions (Fig. 4, E and F). We name this region of the linker domain the PABPC interacting and essential element (PIE). The RRM1 and RRM2 domains of PABPC1 bind the poly(A) RNA directionally, in a 3'-to-5' polarity (73). The PIE-PABPC1 interaction positions RRM1 near the template RNA entry channel of ORF2p. This positioning would allow PABPC1-bound RNA to enter the RT active site in the proper orientation necessary to pair with a target DNA primer strand.

Alanine substitutions of PIE residues severely disrupt activity, which suggests that the ORF2p interaction with PABPC1 is critical for retrotransposition (Fig. 4G). PIE residues are highly conserved across divergent species, particularly toward the PIE C-terminal region, where many of the interactions with RRM1 occur (fig. S13D, residues 285 to 297). When wild-type ORF2p was overexpressed in HEK293T cells, it colocalized with PABPC in cytoplasmic puncta (Fig. 4H, arrows, and fig. S13E, arrows). How-

ever, overexpression of ORF2p carrying PIE site mutation disrupted this colocalization because PABPC did not localize to ORF2p puncta (Fig. 4H and fig. S13E). Taken together, these observations suggest that PABPC1 binding is a fundamental aspect of LINE-1 retrotransposition and may possibly help mediate LINE-1 cis-preference (see Discussion).

Discussion

In this work, we present the structure of a human LINE-1 RNP stalled at TPRT, providing a molecular view into the process that has written nearly 30% of our genomes. Our work not only provides key insights into the mechanism of TPRT, but also into other areas of LINE-1 retrotransposition. This allows us to propose a retrotransposition model that accounts for several previously unclear aspects, which is summarized in Fig. 5.

The LINE-1 machinery preferentially acts on its own mRNA, a characteristic known as cis-preference (74). Although cis-preference requires a poly(A) tail and is thought to occur cotranslationally (52, 75), how ORF2p selects its own mRNA has been unclear. PABPC1 binding to the PIE motif at the N terminus of nascent ORF2p (Fig. 1A) would establish cis-preference cotranslationally and may facilitate RNP formation by positioning the RNA for cofolding with ORF2p (Fig. 5, step 1). This is consistent with previous studies showing that PABPC1 depletion causes a defect in LINE-1 RNP formation (53). Additionally, PABPCs multimerize across the poly(A) tail (76, 77), which limits access to all but the most distal RRM1 domain near the mRNA 3' end. ORF2p-RRM1 binding would then position ORF2p near the mRNA 3' end (Fig. 5, step 1, red arrow) and may protect the LINE-1 mRNA from deadenylation, similar to the LARPI-PABPC complex (78). Protecting against deadenylation may ensure that the LINE-1 mRNA maintains a long poly(A) tract—a feature that coincides with retrotransposition potential (52, 79).

Although the physiological requirements for LINE-1 TPRT are still unclear, several lines of evidence indicate that the DNA architecture is critical to target DNA selection. First, bottom strand nicking and TPRT are nearly undetectable on double-stranded target DNA substrates (Fig. 1E, lane 2). Second, retrotransposition appears to be linked to DNA replication (55, 80–82). Third, DNA substrates that mimic replication intermediates strongly stimulate EN bottom strand nicking (26). It is important to note that our TPRT complex assembly approach bypasses bottom strand nicking of TPRT. Therefore, we lack structural insights into the early stages of ORF2p engagement with the target DNA and any potential DNA architectural requirements critical for this process.

It is possible that ORF2p exploits PCNA to find a target DNA with a suitable architecture

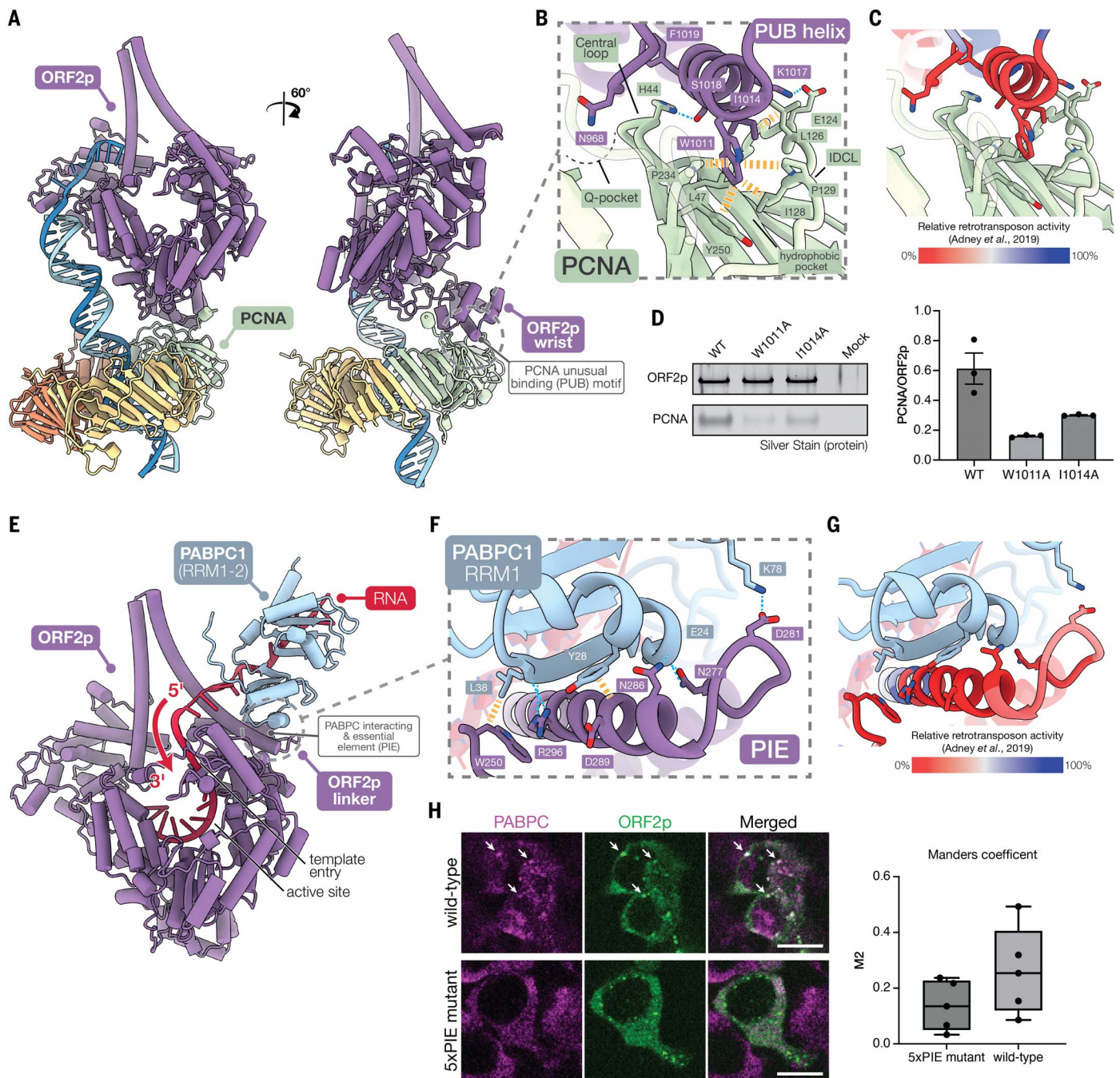


Fig. 4. Cellular factors facilitate nucleic acid binding. (A) AlphaFold 3 prediction of the ORF2p-PCNA complex. (B) Detailed view of the predicted interaction between the PUB motif and PCNA. (C) Effect of PUB trialanine substitutions on retrotransposition efficiency. The same view as in (B) is shown, with retrotransposition efficiencies from trialanine scanning substitutions (50) mapped onto the structure. (D) Silver-stained SDS-PAGE from ORF2p pull-down experiments with PUB site mutants (left) and quantification of the pull-down experiments (right). The experiments were performed in triplicate ($n = 3$). Values represent PCNA band intensity normalized to ORF2p band intensity. Error bars represent SEMs. WT, wild-type. (E) AlphaFold 3

prediction of the ORF2p-PABPC1 complex. (F) Detailed view of the interactions between the PIE region of ORF2p and PABPC1. (G) Effect of PIE trialanine substitutions on retrotransposition efficiency. The same view as in (F) is shown, with retrotransposition efficiencies from trialanine scanning substitutions (50) mapped onto the structure. (H) (Left) Immunofluorescence staining of ORF2p (wild-type or 5xPIE mutant; green) and PABPC (magenta). Arrows indicate examples of ORF2p cytoplasmic puncta colocalized with PABPC, which were not observed in the ORF2p 5xPIE mutant. 5xPIE mutant: M272A, N277A, D281A, N286A, and R296A. Scale bar, 10 μ m. (Right) Quantification of Manders coefficients ($n = 10$).

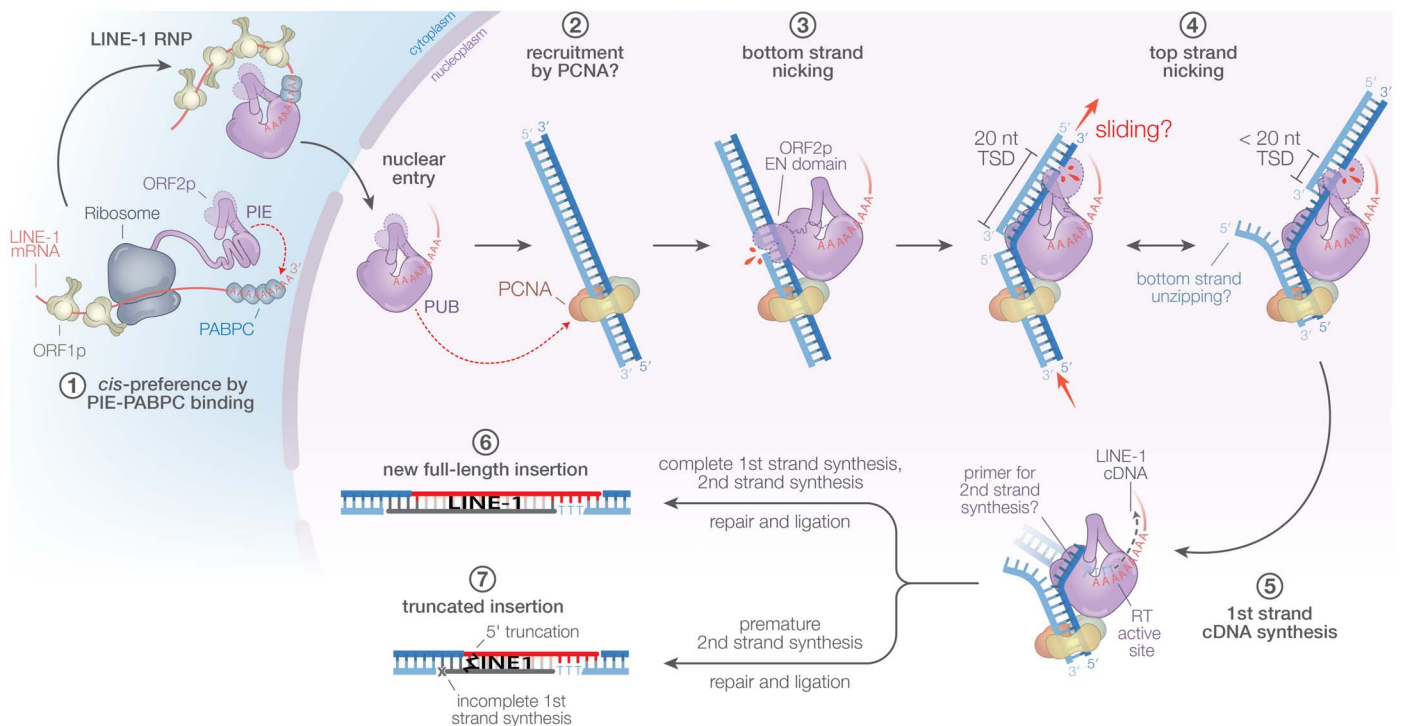


Fig. 5. Model for TPRT and LINE-1 retrotransposition. (1) Cotranslational ORF2p PIE-PABPC binding establishes cis-preference. (2) After RNP formation and nuclear entry, PCNA recruits the LINE-1 RNP to a target DNA with the appropriate architecture for retrotransposition. (3) EN domain nicks the bottom strand at a site resembling the EN cleavage consensus motif. (4) Sliding and unzipping of the target DNA allows the EN domain to nick the top strand at a suitable site and explains the observed distribution of TSD

lengths. The timing of top strand nicking is unclear. (5) First-strand cDNA synthesis initiates after the bottom strand is passed to the RT active site and anneals with the poly(A) tail. (6) Complete first-strand synthesis followed by template jumping to the exposed top strand initiates second-strand synthesis and results in a new full-length insertion. (7) Premature second-strand synthesis before first-strand synthesis has completed would lead to a new 5' truncated insertion.

(Fig. 5, step 2). The predicted interaction between ORF2p and PCNA is far more extensive than the typical PIP box-PCNA interaction with canonical PCNA binding partners. This may allow ORF2p to outcompete or displace these factors for PCNA binding. It is not so surprising that ORF2p uses host factors for retrotransposition by binding to conserved binding sites. This would prevent the host from escaping retrotransposition by mutating these sites (83).

The nucleic acid architecture observed in our TPRT structure provides broader insights into the pathway of LINE-1 retrotransposition. Although it is assumed that ORF2p nicks the top strand to initiate second-strand synthesis, the exact mechanism has been unclear. Our findings show that ORF2p not only nicks the top strand but also rearranges the target DNA into a state that appears primed for second-strand synthesis—all before or during first-strand synthesis (Fig. 5, step 5). This contrasts a recently proposed model in which ORF2p remodels a template RNA duplex and does not nick the top strand, instead relying on replication intermediates to generate a primer for second-strand synthesis (26).

Although these models are not mutually exclusive, our structure suggests a pathway that

explains the variability in TSD length and may account for the structural sequence variations observed at LINE-1 insertions events, particularly 5' truncations (42, 43, 45, 47). Nicking of the top strand provides the primer needed for second-strand synthesis before the completion of first-strand synthesis (Fig. 5, step 5). Initiating second-strand synthesis after completing first-strand synthesis would result in a new full-length LINE-1 insertion (Fig. 5, step 6). Alternatively, a premature transition to second-strand synthesis would result in 5' truncated insertions (Fig. 5, step 7).

Materials and methods

ORF2p purification

A codon-optimized human ORF2p sequence (a gift from D. Rio) was cloned into the pACEBac1 transfer vector containing an N-terminal 8xHis-TwinStrep-MBP-SUMO* tag. Baculoviruses were generated using the Bac-to-Bac Baculovirus expression system (Invitrogen) and EmBacY cells (Geneva Biotech) (83). For expression, 1 liter of *Trichoplusia ni* High Five at a density of 1.0×10^6 cells/ml was infected with 10 ml of high titer baculovirus stock. Infected cells were grown for 72 hours at 27°C, harvested by centrifugation, snap

frozen in liquid nitrogen, and stored at -70°C until lysis.

For lysis, cell pellets were thawed and resuspended in hypotonic lysis buffer [20 mM HEPES-NaOH pH 8.0, 2 mM MgCl_2 , 10 μM ZnCl_2 , 0.2 mM EGTA, 10% glycerol, 0.1% IGEPAL CA-630, 1 mM dithiothreitol (DTT), 1 mM phenylmethylsulfonyl fluoride (PMSF), 1 cOmplete Protease Inhibitor Cocktail tablet/50 ml (Roche)]. Extracts were prepared by three freeze-thaw cycles and clarified by centrifugation after adjusting the salt concentration to 300 mM with 5 M NaCl. Clarified extracts were adjusted to 150 mM NaCl by dilution followed by snap freezing in liquid nitrogen and storage at -70°C until purification.

ORF2p was purified from extracts by a two-step procedure. First, extracts were thawed, supplemented with 15 $\mu\text{l/ml}$ of BioLock (IBA LifeSciences) and 1/10 volume 4 M $(\text{NH}_4)_2\text{SO}_4$, and then passed through a 0.22 μm syringe filter. Filtrates were applied on to 5 ml of pre-equilibrated Strep-Tactin XT Sepharose (Cytiva) by gravity flow. The resin was washed three times with 10 column volumes (CVs) of O2 buffer [25 mM HEPES-NaOH pH 8.0, 400 mM $(\text{NH}_4)_2\text{SO}_4$, 1 mM MgCl_2 , 10 μM ZnCl_2 , 1 mM DTT, 1 mM PMSF], once with 5 CVs of

A2 buffer (O2 buffer supplemented to 500 mM with L-arginine HCl), and finally eluted three times in batch with 1 CV of E2 buffer (O2 buffer supplemented to 500 mM L-arginine HCl and 50 mM biotin).

Next, the salt concentration was adjusted to 100 mM by dilution before application onto a 1 ml HiTrap SP HP cation exchange column (Cytiva) pre-equilibrated in IEX A buffer [25 mM HEPES-NaOH pH 8.0, 100 mM $(\text{NH}_4)_2\text{SO}_4$, 1 mM MgCl_2 , 10 μM ZnCl_2 , 1 mM DTT, 1 mM PMSF] and then eluted with a linear gradient to 1.2 M $(\text{NH}_4)_2\text{SO}_4$. Fractions with the highest specific activity (typically a single 200 μl fraction) were supplemented to 10% with glycerol, aliquoted, snap frozen in liquid nitrogen, and stored at -70°C until use in biochemical assays. For structural determination, fractions were immediately used for complex formation and cryo-EM sample preparation. Protein concentration was determined by densitometry.

PCNA purification

Human PCNA with an N-terminal polyhistidine SUMO tag expression plasmid was transformed into BL21(DE3) *Escherichia coli* strain. Two liters of cells were cultured at 37°C in 2xTY medium to an OD of 0.6, then induced with 0.8 mM IPTG followed by a 3 hours incubation at 37°C . Cells were harvested, resuspended in IMAC A buffer (50 mM Tris-HCl pH 8.0, 300 mM NaCl, 0.01% IGEPAL CA-630, 30 mM imidazole, 0.5 mM DTT, 1 mM PMSF), sonicated, and clarified by centrifugation for 30 min at 4°C and 25,000g. The lysate was filtered and applied to a 5 ml HisTrap HP column (Cytiva). The column was washed with IMAC A before elution with a linear gradient to IMAC A supplemented with imidazole to 500 mM. The tag was cleaved overnight with SUMO protease (LifeSensors).

The salt concentration was adjusted to 150 mM by dilution before application onto a 1 ml HiTrap Q HP anion exchange column (Cytiva) pre-equilibrated in IEX A buffer (25 mM Tris-HCl pH 7.4, 150 mM NaCl, 10% glycerol, 0.5 mM DTT, 1 mM PMSF) and eluted with a linear gradient to 1.0 M NaCl. The eluate was supplemented with imidazole to 35 mM and applied to 3.0 ml of Ni Sepharose HP resin (Cytiva) to remove the tag and uncleaved PCNA.

PCNA was further purified using a HiLoad Superdex 200 size exclusion column (Cytiva) in SEC buffer (25 mM Tris-HCl pH 7.4, 300 mM NaCl, 10% glycerol, 0.5 mM DTT, 1 mM PMSF). Peak fractions were pooled, concentrated to 70 μM , aliquoted, flash-frozen in liquid nitrogen, and stored at -80°C .

ORF2p pull-down with PCNA

Insect cells were infected with ORF2p mutants and lysed as described above. Extracts were thawed, supplemented with 15 $\mu\text{l}/\text{ml}$ of BioLock

(IBA LifeSciences), 1/10 volume 4 M $(\text{NH}_4)_2\text{SO}_4$, and then passed through a 0.22 μm syringe filter. 1.5 ml of filtrates were incubated in batch with 200 μl of MagStrep Strep-Tactin beads (5% suspension, IBA LifeSciences) for 30 min at 4°C . The resin was washed three times with 1.0 ml of O2 buffer, then washed twice with binding buffer [25 mM HEPES-NaOH pH 8.0, 150 mM KOAc, 1.5 mM $\text{Mg}(\text{OAc})_2$, 10 μM ZnCl_2 , 1 mM DTT, 0.5 mM PMSF]. The resin was incubated in batch with 0.25 μM PCNA in 100 μl binding buffer for 30 min at 4°C . The resin was then washed three times with 0.8 ml binding buffer and eluted in batch at 22°C with 30 μl binding buffer supplemented with 50 mM biotin. Fractions were analyzed by silver stained SDS-polyacrylamide gel electrophoresis (SDS-PAGE) and quantified using Image J (version 2.14.0). The experiments were performed in three independent technical replicates.

Preparation of RNA substrates

For the *AluYa5* RNA substrate, a 5 ml in vitro transcription (IVT) reaction was prepared from a *NheI*-linearized plasmid template of the *Alu* RNA including a 55 nt poly(A) sequence. IVT reactions composed of 4 mM of each adenosine triphosphate (ATP), cytidine triphosphate (CTP), guanosine triphosphate (GTP), and uridine triphosphate (UTP); 40 mM Tris HCl pH 8.0; 30 mM MgCl_2 ; 2 mM spermidine; 10 mM DTT; 200 $\mu\text{g}/\text{ml}$ DNA template; and 15 $\mu\text{g}/\text{ml}$ of homemade T7 RNA polymerase. The reaction was incubated overnight at 37°C . The magnesium pyrophosphate precipitate was pelleted and removed by centrifugation, followed by the addition of 50 U of RQ1 ribonuclease (RNase)-free deoxyribonuclease (DNase) (Promega), and incubation at 37°C for 1 hour. The RNA was extracted twice with acidic phenol: chloroform:isoamyl alcohol, supplemented with 1/10 volume of 3 M NaOAc pH 5.2, then precipitated by the addition of 2.5 volumes of 100% ethanol followed by overnight incubation at -20°C . The RNA pellet was washed twice with 70% ethanol, dried, resuspended in TE (10 mM Tris-HCl pH 8.0, 10 mM EDTA), aliquoted, and stored at -70°C until use.

pA₃₀ RNA oligonucleotides were synthesized by IDT. The sequences of the RNA substrates used in this study are listed in table S2.

Preparation of DNA substrates

Target DNA sequences were derived from de novo LINE-1 insertions into exon 14 of the human factor VIII gene (27). This target DNA sequence was idealized to extend the region of complementarity with the poly(A) tail. DNA oligonucleotides were synthesized by IDT and resuspended in IX Annealing buffer (10 mM HEPES-NaOH pH 8.0, 60 mM KCl). Where necessary, DNA oligonucleotides were purified by preparative denaturing PAGE.

Equimolar ratios of target DNA strands were mixed at 25 μM final concentration, then annealed by heating to 98°C for 5 min in a heat block and allowed to cool overnight to ambient temperature. Sequences of DNA oligonucleotides used in this study are listed in table S2.

In vitro TPRT assays

TPRT reactions were carried out in 20 μl volumes and were typically composed of 50 nM labeled target DNA, 1 μM RNA in 25 mM HEPES-NaOH pH 8.0, 500 mM KOAc, 1.5 mM $\text{Mg}(\text{OAc})_2$, 10 μM $\text{Zn}(\text{OAc})_2$, 1 mM DTT, and 25 μM of each dNTP. Reactions were initiated by the addition of 1 to 5 μl of ORF2p protein (to a final concentration of 7.5 to 37.5 nM) and incubated at 37°C for 1 hour. Reactions were stopped by adding 1 μl of 20x STOP mix I (1 mg/ml RNase A, 120 mM EDTA). For experiments in Fig. 3, reactions were stopped by adding 1 μl of 20x STOP mix II (2% SDS, 200 mM EDTA) and 1 μg RNase A per reaction. RNA was digested for 20 min at room temperature and incubated at 37°C for 30 min after adding 10 μg proteinase K per reaction.

One volume of 2x loading buffer (95% deionized formamide, 0.02% SDS, 1 mM EDTA) was added to each sample, followed by the addition of 1/20 volume of 100 mM NaOH, before boiling for 5 min. Reactions were resolved by 12% denaturing PAGE run at 10 W for 10 to 25 min. Gels were visualized on a Typhoon Imager (Cytiva).

Target DNA substrates used in TPRT assays typically had a 5' fluorescein modification (6-FAM) on the bottom strand. For experiments in Fig. 3, target DNA substrates were modified with 5' fluorescein on the top strand and 5' Cy5 on the bottom strand.

Mapping top strand cleavage sites

To map the top strand cleavage sites in Fig. 3A, TPRT products were compared with a top strand sequencing ladder generated with Terminator (NEB) and dideoxynucleoside triphosphates (ddNTPs, Roche). Briefly, sequencing ladder reactions composed of 20 nM 5' 6-FAM labeled top strand primer, 10 nM bottom strand template, 1x ThermoPol buffer (NEB), 0.02 U/ μl Terminator DNA polymerase (NEB), 0.02 U/ μl thermostable inorganic pyrophosphatase (NEB), 100 μM dNTPs, and one ddNTP per reaction (5 μM ddATP; 5 μM ddTTP; 2.5 μM ddCTP; or 2.5 μM ddGTP) in a volume of 20 μl . Reactions were incubated in a thermocycler at 94°C for 10 min, followed by 25 cycles of 94°C for 30 s, 55°C for 30 s, and 72°C for 1 min, followed by one cycle at 72°C for 1 min.

Reactions were brought up to 200 μl with standard TE buffer, extracted once with phenol:chloroform:isoamyl alcohol, and supplemented with 20 μl of 3M NaOAc and 20 μl of 20 mg/ml glycogen before precipitation with

2.5 volumes of cold 100% ethanol at -20°C overnight. Samples were pelleted by centrifugation. Pellets were washed once with 70% cold ethanol, pelleted again, dried, and resuspended in $15\ \mu\text{l}$ of 1:1:8 water to 100 mM NaOH to 2x loading buffer. After boiling for 5 min, $5\ \mu\text{l}$ of each sample were resolved on a 12% denaturing PAGE 40 cm \times 0.4 mm sequencing gel run at 25 W for 2 to 3 hours. Gels were visualized on a Typhoon Imager (Cytiva).

Immunofluorescence staining and quantification

HEK293T cells (ATCC, cat. no. CRL-3216, RRID:CVCL_0063) were cultured in DMEM with GlutaMax (ThermoFisher), supplemented with 10% FBS, 100 $\mu\text{g}/\text{ml}$ streptomycin, and 100 unit/ml penicillin. Cells were seeded in 6-well plates on coverslips coated with 0.1% poly-L-lysine (Sigma-Aldrich, cat. no. P1399) in phosphate-buffered saline (PBS) to 70 to 80% confluency and then transfected with 4 μg of plasmid DNA of either wild-type ORF2p or 5xPIE ORF2p mutant using Lipofectamine 2000 (ThermoFisher, cat. no. 11668027). Wild-type and mutant ORF2p expression constructs carried a C-terminal Strep tag. After 24 hours, the transfected cells were washed with PBS twice, fixed using cold 4% paraformaldehyde in PBS for 20 min and washed with PBS again twice. Cells were permeabilized by incubation with 0.5% v/v Triton X-100 in PBS for 2 min at room temperature and washed three times with PBS. After incubation with blocking buffer [5% bovine serum albumin (BSA) in PBS] for 30 min at room temperature, the cells were incubated with anti-Strep (Abcam ab252885, 1:1000) and anti-PABP (Abcam ab312314, 1:250) in blocking buffer overnight at 4°C . The cells were washed three times with PBS and incubated with goat anti-rat Alexa-Fluor 488 (Abcam, ab150165, 1:1000) and goat anti-rabbit Alexa-Fluor 647 (Life Technologies A21245, lot 1752070, 1:1000) in PBST for 1 hour in the dark at room temperature. After washing three times with PBS, the coverslips were mounted on a glass slide using Vectashield Plus antifade mounting medium with 4',6-diamidino-2-phenylindole (DAPI) (Vector Laboratories, H-2000), sealed, and stored at 4°C until imaging.

The fixed cells were imaged on a Zeiss 780 confocal microscope operated at room temperature. The fluorescence signals were obtained using the 488- and 633-nm lasers. Image stacks were taken with a 63x/0.4NA oil-immersion objective (pixel size = $0.2636\ \mu\text{m}$) using a GaAsP detector every $0.3977\ \mu\text{m}$. The Manders' overlap coefficients were computed using a custom-made ImageJ macro that, for each channel, segmented the blob-like regions using a difference of Gaussian filters with respective sigma 1 and 4 pixels and a threshold set to the mean plus twice the standard deviation of the filtered image. This provided 3D binary masks for each channel from which the co-

efficient was computed as the sum of the intensity of a channel in the intersection of the masks normalized by the sum of intensity in the mask associated to this channel. Boxplots for the coefficients were plotted using Prism 10 (GraphPad).

ORF2p TPRT complex formation for cryo-EM

Our initial attempts to prepare high-quality TPRT complexes for cryo-EM were unsuccessful. ORF2p readily precipitated over the course of complex formation, and a substantial fraction of our protein preparations were still inactive, despite the high specific activity. To overcome these challenges, we purified active TPRT complexes away from inactive ORF2p using a biotinylated prenicked target DNA (fig. S2A). This purification strategy has been successfully used for other challenging nucleoprotein complexes (35, 84).

For assembly of the ORF2p TPRT complex, 50 μl ($\sim 45\ \text{nM}$) of freshly purified high-specific activity ORF2p was supplemented with 90 nM prenicked target DNA sequence and 1 μM 30 nt poly(A) RNA, and dialyzed against dialysis buffer [25 mM HEPES-NaOH pH 8.0, 500 mM KOAc, 1.5 mM $\text{Mg}(\text{OAc})_2$, 10 μM $\text{Zn}(\text{OAc})_2$, 1 mM DTT, 0.5 mM PMSF] at 4°C overnight. The target DNA contained a 5' desthiobiotin-TEG modification on the top strand and 5' fluorescein on the bottom strand. The sample was supplemented with 100 μM of ddTTP and incubated at 37°C for 30 min before binding to streptavidin mag sepharose (Cytiva) for 1 hour at 4°C . The resin was washed twice with dialysis buffer supplemented with 25 μM ddTTP and eluted for 30 min at 37°C with dialysis buffer supplemented with 25 μM ddTTP and 50 mM biotin. Eluted complexes were immediately used for vitrification.

Cryo-EM grid preparation and data collection

Vitrification was performed using a Vitrobot Mark IV (ThermoFisher Scientific) maintained at 4°C and 100% humidity. 3 μl of ORF2p TPRT complex was applied onto freshly glow-discharged (1 s at 40 mA) Quantifoil R 1.2/L3 Au 300 grid, precoated with a layer of graphene oxide by following a published procedure (85, 86). After a 30-s incubation, the grid was blotted for 3 s with a blot force of -10 and subsequently plunged into liquid ethane.

Data collection was performed on a Titan Krios G4 cryo-transmission electron microscope operated at 300 kV with fringe-free imaging and equipped with a C-FEG, Selectris X energy-filter, and a Falcon 4i direct electron detector (ThermoFisher Scientific). 25,374 movies were automatically collected using EPU (ThermoFisher Scientific) in counting mode with a pixel size of $0.955\ \text{\AA}$ over a defocus range of $-0.8\ \mu\text{m}$ to $-2.2\ \mu\text{m}$. We used a flux of $9.45\ \text{e}^-/\text{pixel}/\text{s}$ and an exposure time of 5.85 s, yielding a total fluence of $59.22\ \text{e}^-/\text{\AA}^2$. Each movie was fractionated into

50 movie frames. An energy filter slit width of 10 eV was used.

Cryo-EM data processing

Processing strategy for the consensus reconstruction

Data were processed using RELION-5.0, unless otherwise indicated (fig. S3). 25,374 movies were gain-corrected, dose-weighted, and motion-corrected using the RELION implementation of MotionCor2. Contrast transfer function (CTF) parameters were estimated using CTFFIND-4.1 (87). After manual curation, 25,018 micrographs were split by estimated defocus parameters, resulting in three groups with 9252 (defocus $\leq -2.2\ \mu\text{m}$), 8473 ($-2.2\ \mu\text{m} < \text{defocus} < -1.5\ \mu\text{m}$), and 7293 (defocus $\geq -1.5\ \mu\text{m}$) micrographs, respectively. Particle picking was carried out using Topaz with the general model (88). Particles were extracted from each defocus group using varying figure-of-merit values (-0.5 , -1.0 , and -2.0 , respectively) at a pixel size of $4.46\ \text{\AA}/\text{pixel}$ and box size of 60^2 pixels, yielding 4,568,277 particles.

The particles were first filtered by 3D classification, then filtered by 2D classification without alignment, yielding a subset of 1,371,912 particles. Particles were reextracted at an unbinned pixel size of $0.955\ \text{\AA}/\text{pixel}$ and box size of 280^2 pixels and then refined to $2.72\text{-}\text{\AA}$ resolution. We noticed that this subset contained a substantial number of particles with high defocus values; therefore, we reextracted the particles with an increased box size of 380^2 pixels to capture more signal delocalized by the CTF.

The reextracted particles were classified into six 3D classes without alignment and with a regularization parameter T of 24. We combined five classes with well-defined, high-resolution features, yielding a subset of 680,273 particles, which we then refined to $2.62\text{-}\text{\AA}$ resolution. Iterative rounds of CTF refinement (beam tilt, trefoil, and fourth-order aberrations; anisotropic magnification; per-particle defocus, and per-micrograph astigmatism) (89), 3D refinement, and Bayesian polishing (90) culminated in a consensus reconstruction at $2.27\text{-}\text{\AA}$ resolution.

Processing strategy for the open fingers and closed fingers reconstructions

We noticed characteristics of varying occupancies in the density around the active site of the consensus reconstruction. Therefore, the particles were imported to CryoSPARC v4.5.3 for nonuniform refinement and 3D classification with mask surrounding the active site (fig. S3) (91, 92). To resolve the open fingers state, particles from the nonuniform refinement were subject to focused 3D classification into four classes, initialized by principal components analysis (PCA), at a target resolution of $3\ \text{\AA}$. A subset of 183,579 particles showed well-defined density for the fingers in the open configuration.

To resolve the closed fingers state, particles from the nonuniform refinement were subject to focused 3D classification as above, except with a class similarity parameter of 0.1 and an input initialization mode. This produced one class with well-defined density for the fingers in the closed configuration and strong occupancy of the ddTTP in the active site, corresponding to a subset of 185,228 particles.

Each subset was prepared for downstream processing in RELION using an in-house Python script that implements PyEM (93) and Starparser (94). This yields a subset from the original RELION .star file, corresponding to the particles classified in CryoSPARC. The resulting .star files were imported into RELION and refined to 2.45-Å resolution and 2.50-Å resolution for the open fingers state and closed fingers state, respectively.

Processing strategy for EN-resolved reconstruction

During the above analysis, we noticed weak density in some of the classes that could correspond to the EN domain. Therefore, we imported the original 1,371,912 particle subset from RELION, into CryoSPARC for nonuniform refinement and focused 3D classification with a generous mask near the linker domain (fig. S11A). The 3D classification was initialized using four volumes and a filter resolution of 16 Å. One class, consisting of 443,253 particles, displayed strong EN density and was reimported into RELION using the strategy described above. Particles were reextracted at bin 2 to speed up calculations, then subject to focused 3D classification without alignment and with a regularization parameter T of 250. A class with 121,941 particles with the best-resolved EN density was subsequently refined to 3.18 Å. CTF refinement (beam tilt, trefoil, and fourth-order aberrations; anisotropic magnification, per-particle defocus, and per-micrograph astigmatism) followed by Bayesian polishing and 3D refinement with Blush regularization (48) yielded a final 3.1-Å reconstruction. Multibody refinement was used to characterize the flexibility of the EN domain (fig. S11F) (95). The position of the EN domain was “fixed” during multibody refinement by setting the widths of the rotational and translational priors set to zero (96).

For all maps, resolutions are reported using the gold-standard Fourier shell correlation (FSC) = 0.143 criterion (fig. S4A; fig. S7, A and B; and fig. S11B). B-factors were determined by RELION or from a user-defined value (table S1). Local resolutions were calculated in RELION (fig. S4D; fig. S7, G and H; and fig. S11E). Directional FSC plots and sphericity values were calculated using a 3D-FSC webserver (fig. S4B; fig. S7, C and D; and fig. S11C) (<https://3dfsc.salk.edu/>) (97). Particle orientation plots (Euler angles) were calculated using a Python script

(fig. S4C; fig. S7, E and F; and fig. S11D) (<https://github.com/Guillaume/angdist>).

Model building, refinement, and AlphaFold3 prediction

An AlphaFold2 (98) prediction was used as an initial model for model building into the consensus, open, and closed fingers maps. The model was first adjusted into the map in ISOLDE 1.8 (99), then adjusted in COOT 0.9.8.92 (100). Nucleic acid models were generated in COOT, then adjusted into the map using ISOLDE. The model for ddTTP was imported from the REFMAC monomer library in COOT. To allow map blurring and sharpening in COOT, maps were converted from MRC format into MTZ format using REFMAC5.8 (101). ISOLDE and COOT were iteratively used to diagnose and fix errors and to improve model geometry. For the EN-resolved model, model building was carried out as described above but included adaptive distance and torsion restraints in ISOLDE for the EN domain using a crystal structure [Protein Data Bank (PDB) ID: 1VYB] (49) as a reference.

Models were first refined using PHENIX 1.21.1-5286 (102) then Servalcat 0.4.72 (103). All PHENIX refinements were limited to one macrocycle of global minimization and atomic displacement parameter (ADP) refinement, using a parameter file generated in ISOLDE. Servalcat refinements included protein secondary structure restraints and nucleic acid restraints calculated using PROSMART and LIBG, respectively (104, 105). Model-versus-map FSCs and EMRinger scores were calculated using PHENIX. Q-scores were calculated in UCSF ChimeraX (106). Model geometries were assessed using the MolProbity server (<http://molprobity.biochem.duke.edu/>). A summary of the refined models is provided in table S2. The identity of bases in the second primer region and in the “unassigned nucleic acid” could not be unambiguously assigned. Therefore, we have modeled these bases as either A or T.

AlphaFold3 (59) predictions were performed using the webserver interface (<https://alphafoldserver.com/>) with a randomly generated seed. Predicted aligned error (PAE) plots were generated using a modified Python script (<https://github.com/nayimgr/af3analysis>). Sequences used for AlphaFold3 predictions in Fig. 4 are included in table S2.

Map and model visualization

Maps and models were visualized with UCSF ChimeraX. Illustrations were prepared using Adobe Illustrator, ChimeraX, and PyMOL (<https://www.pymol.org/>).

Sequence alignments

Protein sequences for sequence alignment were downloaded from UniProt (107) or from

Boissinot and Sookdeo (108) and aligned using Clustal Omega (109).

REFERENCES AND NOTES

- J. D. Boeke, D. J. Garfinkel, C. A. Styles, G. R. Fink, Ty elements transpose through an RNA intermediate. *Cell* **40**, 491–500 (1985). doi: [10.1016/0092-8674\(85\)90197-7](https://doi.org/10.1016/0092-8674(85)90197-7); pmid: [2982495](https://pubmed.ncbi.nlm.nih.gov/2982495/)
- International Human Genome Sequencing Consortium, Initial sequencing and analysis of the human genome. *Nature* **409**, 860–921 (2001). doi: [10.1038/35057062](https://doi.org/10.1038/35057062); pmid: [11237011](https://pubmed.ncbi.nlm.nih.gov/11237011/)
- B. Brouha *et al.*, Hot L1s account for the bulk of retrotransposition in the human population. *Proc. Natl. Acad. Sci. U.S.A.* **100**, 5280–5285 (2003). doi: [10.1073/pnas.0831042100](https://doi.org/10.1073/pnas.0831042100); pmid: [12682288](https://pubmed.ncbi.nlm.nih.gov/12682288/)
- C. R. Beck *et al.*, LINE-1 retrotransposition activity in human genomes. *Cell* **141**, 1159–1170 (2010). doi: [10.1016/j.cell.2010.05.021](https://doi.org/10.1016/j.cell.2010.05.021); pmid: [20602998](https://pubmed.ncbi.nlm.nih.gov/20602998/)
- D. M. Sassaman *et al.*, Many human L1 elements are capable of retrotransposition. *Nat. Genet.* **16**, 37–43 (1997). doi: [10.1038/ng0597-37](https://doi.org/10.1038/ng0597-37); pmid: [9140393](https://pubmed.ncbi.nlm.nih.gov/9140393/)
- J. V. Moran *et al.*, High frequency retrotransposition in cultured mammalian cells. *Cell* **87**, 917–927 (1996). doi: [10.1016/S0092-8674\(00\)81998-4](https://doi.org/10.1016/S0092-8674(00)81998-4); pmid: [8945518](https://pubmed.ncbi.nlm.nih.gov/8945518/)
- D. C. Hanczian, H. H. Kazazian Jr., Roles for retrotransposon insertions in human disease. *Mob. DNA* **7**, 9 (2016). doi: [10.1186/s13100-016-0065-9](https://doi.org/10.1186/s13100-016-0065-9); pmid: [27158268](https://pubmed.ncbi.nlm.nih.gov/27158268/)
- K. H. Burns, Transposable elements in cancer. *Nat. Rev. Cancer* **17**, 415–424 (2017). doi: [10.1038/nrc.2017.35](https://doi.org/10.1038/nrc.2017.35); pmid: [28642606](https://pubmed.ncbi.nlm.nih.gov/28642606/)
- V. Gorbunova *et al.*, The role of retrotransposable elements in ageing and age-associated diseases. *Nature* **596**, 43–53 (2021). doi: [10.1038/s41586-021-03542-y](https://doi.org/10.1038/s41586-021-03542-y); pmid: [34349292](https://pubmed.ncbi.nlm.nih.gov/34349292/)
- P. J. Enyeart, G. Mohr, A. D. Ellington, A. M. Lambowitz, Biotechnological applications of mobile group II introns and their reverse transcriptases: Gene targeting, RNA-seq, and non-coding RNA analysis. *Mob. DNA* **5**, 2 (2014). doi: [10.1186/1759-8753-5-2](https://doi.org/10.1186/1759-8753-5-2); pmid: [24410776](https://pubmed.ncbi.nlm.nih.gov/24410776/)
- J. Strecker *et al.*, RNA-guided DNA insertion with CRISPR-associated transposases. *Science* **365**, 48–53 (2019). doi: [10.1126/science.aax9181](https://doi.org/10.1126/science.aax9181); pmid: [31171706](https://pubmed.ncbi.nlm.nih.gov/31171706/)
- G. D. Lampe *et al.*, Targeted DNA integration in human cells without double-strand breaks using CRISPR-associated transposases. *Nat. Biotechnol.* **42**, 87–98 (2024). doi: [10.1038/s41587-023-01748-1](https://doi.org/10.1038/s41587-023-01748-1); pmid: [36991112](https://pubmed.ncbi.nlm.nih.gov/36991112/)
- S. E. Klompe, P. L. H. Vo, T. S. Halpin-Healy, S. H. Sternberg, Transposon-encoded CRISPR-Cas systems direct RNA-guided DNA integration. *Nature* **571**, 219–225 (2019). doi: [10.1038/s41586-019-1323-z](https://doi.org/10.1038/s41586-019-1323-z); pmid: [31189177](https://pubmed.ncbi.nlm.nih.gov/31189177/)
- S. C. Pimentel, H. E. Upton, K. Collins, Separable structural requirements for cDNA synthesis, nontemplated extension, and template jumping by a non-LTR retroelement reverse transcriptase. *J. Biol. Chem.* **298**, 101624 (2022). doi: [10.1016/j.jbc.2022.101624](https://doi.org/10.1016/j.jbc.2022.101624); pmid: [35065960](https://pubmed.ncbi.nlm.nih.gov/35065960/)
- X. Zhang *et al.*, Harnessing eukaryotic retroelement proteins for transgene insertion into human safe-harbor loci. *Nat. Biotechnol.* **43**, 42–51 (2025). doi: [10.1038/s41587-024-02137-y](https://doi.org/10.1038/s41587-024-02137-y); pmid: [38379101](https://pubmed.ncbi.nlm.nih.gov/38379101/)
- D. A. Kulpa, J. V. Moran, Cis-preferential LINE-1 reverse transcriptase activity in ribonucleoprotein particles. *Nat. Struct. Mol. Biol.* **13**, 655–660 (2006). doi: [10.1038/nsmb1107](https://doi.org/10.1038/nsmb1107); pmid: [16783376](https://pubmed.ncbi.nlm.nih.gov/16783376/)
- D. A. Kulpa, J. V. Moran, Ribonucleoprotein particle formation is necessary but not sufficient for LINE-1 retrotransposition. *Hum. Mol. Genet.* **14**, 3237–3248 (2005). doi: [10.1093/hmg/ddi354](https://doi.org/10.1093/hmg/ddi354); pmid: [16183655](https://pubmed.ncbi.nlm.nih.gov/16183655/)
- S. L. Martin *et al.*, LINE-1 retrotransposition requires the nucleic acid chaperone activity of the ORF1 protein. *J. Mol. Biol.* **348**, 549–561 (2005). doi: [10.1016/j.jmb.2005.03.003](https://doi.org/10.1016/j.jmb.2005.03.003); pmid: [15826653](https://pubmed.ncbi.nlm.nih.gov/15826653/)
- Q. Feng, J. V. Moran, H. H. Kazazian Jr., J. D. Boeke, Human L1 retrotransposon encodes a conserved endonuclease required for retrotransposition. *Cell* **87**, 905–916 (1996). doi: [10.1016/S0092-8674\(00\)81997-2](https://doi.org/10.1016/S0092-8674(00)81997-2); pmid: [8945517](https://pubmed.ncbi.nlm.nih.gov/8945517/)
- S. L. Mathias, A. F. Scott, H. H. Kazazian Jr., J. D. Boeke, A. Gabriel, Reverse transcriptase encoded by a human transposable element. *Science* **254**, 1808–1810 (1991). doi: [10.1126/science.1722352](https://doi.org/10.1126/science.1722352); pmid: [1722352](https://pubmed.ncbi.nlm.nih.gov/1722352/)
- D. D. Luan, M. H. Korman, J. L. Jakubczak, T. H. Eickbush, Reverse transcription of R2Bm RNA is primed by a nick at the chromosomal target site: A mechanism for non-LTR retrotransposition. *Cell* **72**, 595–605 (1993). doi: [10.1016/0092-8674\(93\)90078-5](https://doi.org/10.1016/0092-8674(93)90078-5); pmid: [7679954](https://pubmed.ncbi.nlm.nih.gov/7679954/)

22. J. Jurka, Sequence patterns indicate an enzymatic involvement in integration of mammalian retroposons. *Proc. Natl. Acad. Sci. U.S.A.* **94**, 1872–1877 (1997). doi: [10.1073/pnas.94.5.1872](https://doi.org/10.1073/pnas.94.5.1872); pmid: [9050872](https://pubmed.ncbi.nlm.nih.gov/9050872/)
23. S. T. Szak *et al.*, Molecular archeology of L1 insertions in the human genome. *Genome Biol.* **3**, research0052.1 (2002). doi: [10.1186/gb-2002-3-10-research0052](https://doi.org/10.1186/gb-2002-3-10-research0052); pmid: [12372140](https://pubmed.ncbi.nlm.nih.gov/12372140/)
24. K. K. Kojima, Different integration site structures between L1 protein-mediated retrotransposition in *cis* and retrotransposition in *trans*. *Mob. DNA* **1**, 17 (2010). doi: [10.1186/1759-8753-1-17](https://doi.org/10.1186/1759-8753-1-17); pmid: [20615209](https://pubmed.ncbi.nlm.nih.gov/20615209/)
25. E. T. Baldwin *et al.*, Structures, functions and adaptations of the human LINE-1 ORF2 protein. *Nature* **626**, 194–206 (2024). doi: [10.1038/s41586-023-06947-z](https://doi.org/10.1038/s41586-023-06947-z); pmid: [38096902](https://pubmed.ncbi.nlm.nih.gov/38096902/)
26. A. Thawani, A. J. F. Ariza, E. Nogales, K. Collins, Template and target-site recognition by human LINE-1 in retrotransposition. *Nature* **626**, 186–193 (2024). doi: [10.1038/s41586-023-06933-5](https://doi.org/10.1038/s41586-023-06933-5); pmid: [38096901](https://pubmed.ncbi.nlm.nih.gov/38096901/)
27. H. H. Kazazian Jr. *et al.*, Haemophilia A resulting from *de novo* insertion of L1 sequences represents a novel mechanism for mutation in man. *Nature* **332**, 164–166 (1988). doi: [10.1038/332164a0](https://doi.org/10.1038/332164a0); pmid: [2831458](https://pubmed.ncbi.nlm.nih.gov/2831458/)
28. G. J. Cost, Q. Feng, A. Jacquier, J. D. Boeke, Human L1 element target-primed reverse transcription *in vitro*. *EMBO J.* **21**, 5899–5910 (2002). doi: [10.1093/emboj/cdf592](https://doi.org/10.1093/emboj/cdf592); pmid: [12411507](https://pubmed.ncbi.nlm.nih.gov/12411507/)
29. S. Viollet, C. Monot, G. Cristofari, L1 retrotransposition: The snap-velcro model and its consequences. *Mob. Genet. Elements* **4**, e28907 (2014). doi: [10.4161/mge.28907](https://doi.org/10.4161/mge.28907); pmid: [24818067](https://pubmed.ncbi.nlm.nih.gov/24818067/)
30. C. Monot *et al.*, The specificity and flexibility of fl reverse transcription priming at imperfect T-tracts. *PLOS Genet.* **9**, e1003499 (2013). doi: [10.1371/journal.pgen.1003499](https://doi.org/10.1371/journal.pgen.1003499); pmid: [23675310](https://pubmed.ncbi.nlm.nih.gov/23675310/)
31. R. Craigie, K. Mizuuchi, Transposition of Mu DNA: Joining of Mu to target DNA can be uncoupled from cleavage at the ends of Mu. *Cell* **51**, 493–501 (1987). doi: [10.1016/0092-8674\(87\)90645-3](https://doi.org/10.1016/0092-8674(87)90645-3); pmid: [2822259](https://pubmed.ncbi.nlm.nih.gov/2822259/)
32. H. Savilahti, P. A. Rice, K. Mizuuchi, The phage Mu transpososome core: DNA requirements for assembly and function. *EMBO J.* **14**, 4893–4903 (1995). doi: [10.1002/j.1462-0751.1995.tb00170.x](https://doi.org/10.1002/j.1462-0751.1995.tb00170.x); pmid: [7588618](https://pubmed.ncbi.nlm.nih.gov/7588618/)
33. T. Fanning, M. Singer, The LINE-1 DNA sequences in four mammalian orders predict proteins that conserve homologies to retrovirus proteins. *Nucleic Acids Res.* **15**, 2251–2260 (1987). doi: [10.1093/nar/15.5.2251](https://doi.org/10.1093/nar/15.5.2251); pmid: [3562227](https://pubmed.ncbi.nlm.nih.gov/3562227/)
34. A. M. Lentzsch, J. L. Stamos, J. Yao, R. Russell, A. M. Lambowitz, Structural basis for template switching by a group II intron–encoded non-LTR-retroelement reverse transcriptase. *J. Biol. Chem.* **297**, 100971 (2021). doi: [10.1016/j.jbc.2021.100971](https://doi.org/10.1016/j.jbc.2021.100971); pmid: [34280434](https://pubmed.ncbi.nlm.nih.gov/34280434/)
35. M. E. Wilkinson, C. J. Frangieh, R. K. Macrae, F. Zhang, Structure of the R2 non-LTR retrotransposon initiating target-primed reverse transcription. *Science* **380**, 301–308 (2023). doi: [10.1126/science.adg7883](https://doi.org/10.1126/science.adg7883); pmid: [37023171](https://pubmed.ncbi.nlm.nih.gov/37023171/)
36. G. E. Ghanim *et al.*, Structure of human telomerase holoenzyme with bound telomeric DNA. *Nature* **593**, 449–453 (2021). doi: [10.1038/s41586-021-03415-4](https://doi.org/10.1038/s41586-021-03415-4); pmid: [33883742](https://pubmed.ncbi.nlm.nih.gov/33883742/)
37. T. A. Steitz, DNA polymerases: Structural diversity and common mechanisms. *J. Biol. Chem.* **274**, 17395–17398 (1999). doi: [10.1074/jbc.274.25.17395](https://doi.org/10.1074/jbc.274.25.17395); pmid: [10364165](https://pubmed.ncbi.nlm.nih.gov/10364165/)
38. O. Piskareva, C. Ernst, N. Higgins, V. Schmatchenko, The carboxy-terminal segment of the human LINE-1 ORF2 protein is involved in RNA binding. *FEBS Open Bio* **3**, 433–437 (2013). doi: [10.1016/j.fob.2013.09.005](https://doi.org/10.1016/j.fob.2013.09.005); pmid: [24251107](https://pubmed.ncbi.nlm.nih.gov/24251107/)
39. V. Arinkin, G. Smyslyayev, O. Barabas, Jump ahead with a twist: DNA acrobatics drive transposition forward. *Curr. Opin. Struct. Biol.* **59**, 168–177 (2019). doi: [10.1016/j.sbsi.2019.08.006](https://doi.org/10.1016/j.sbsi.2019.08.006); pmid: [31590109](https://pubmed.ncbi.nlm.nih.gov/31590109/)
40. J. Y. Wang, P. Pausch, J. A. Doudna, Structural biology of CRISPR-Cas immunity and genome editing enzymes. *Nat. Rev. Microbiol.* **20**, 641–656 (2022). doi: [10.1038/s41579-022-00739-4](https://doi.org/10.1038/s41579-022-00739-4); pmid: [35562427](https://pubmed.ncbi.nlm.nih.gov/35562427/)
41. I. Miller *et al.*, Structural dissection of sequence recognition and catalytic mechanism of human LINE-1 endonuclease. *Nucleic Acids Res.* **49**, 11350–11366 (2021). doi: [10.1093/nar/gkab826](https://doi.org/10.1093/nar/gkab826); pmid: [34554261](https://pubmed.ncbi.nlm.nih.gov/34554261/)
42. D. E. Symer *et al.*, Human L1 retrotransposition is associated with genetic instability *in vivo*. *Cell* **110**, 327–338 (2002). doi: [10.1016/S0092-8674\(02\)00839-5](https://doi.org/10.1016/S0092-8674(02)00839-5); pmid: [12176320](https://pubmed.ncbi.nlm.nih.gov/12176320/)
43. N. Zingler *et al.*, Analysis of 5' junctions of human LINE-1 and Alu retrotransposons suggests an alternative model for 5'-end attachment requiring microhomology-mediated end-jointing. *Genome Res.* **15**, 780–789 (2005). doi: [10.1101/gr.3421505](https://doi.org/10.1101/gr.3421505); pmid: [15930490](https://pubmed.ncbi.nlm.nih.gov/15930490/)
44. E. M. Ostertag, H. H. Kazazian Jr., Twin priming: A proposed mechanism for the creation of inversions in L1 retrotransposition. *Genome Res.* **11**, 2059–2065 (2001). doi: [10.1101/gr.205701](https://doi.org/10.1101/gr.205701); pmid: [11731496](https://pubmed.ncbi.nlm.nih.gov/11731496/)
45. N. Gilbert, S. Lutz-Prigge, J. V. Moran, Genomic deletions created upon LINE-1 retrotransposition. *Cell* **110**, 315–325 (2002). doi: [10.1016/S0092-8674\(02\)00828-0](https://doi.org/10.1016/S0092-8674(02)00828-0); pmid: [12176319](https://pubmed.ncbi.nlm.nih.gov/12176319/)
46. J. S. Myers *et al.*, A comprehensive analysis of recently integrated human Ta L1 elements. *Am. J. Hum. Genet.* **71**, 312–326 (2002). doi: [10.1086/341718](https://doi.org/10.1086/341718); pmid: [12070800](https://pubmed.ncbi.nlm.nih.gov/12070800/)
47. N. Gilbert, S. Lutz, T. A. Morrish, J. V. Moran, Multiple fates of L1 retrotransposition intermediates in cultured human cells. *Mol. Cell. Biol.* **25**, 7780–7795 (2005). doi: [10.1128/MCB.25.17.7780-7795.2005](https://doi.org/10.1128/MCB.25.17.7780-7795.2005); pmid: [16107723](https://pubmed.ncbi.nlm.nih.gov/16107723/)
48. D. Kimanius *et al.*, Data-driven regularization lowers the size barrier of cryo-EM structure determination. *Nat. Methods* **21**, 1216–1221 (2024). doi: [10.1038/s41592-024-02304-8](https://doi.org/10.1038/s41592-024-02304-8); pmid: [38862790](https://pubmed.ncbi.nlm.nih.gov/38862790/)
49. O. Weichenrieder, K. Repanas, A. Perrakis, Crystal structure of the targeting endonuclease of the human LINE-1 retrotransposon. *Structure* **12**, 975–986 (2004). doi: [10.1016/j.str.2004.04.011](https://doi.org/10.1016/j.str.2004.04.011); pmid: [15274918](https://pubmed.ncbi.nlm.nih.gov/15274918/)
50. E. M. Adney *et al.*, Comprehensive Scanning Mutagenesis of Human Retrotransposon LINE-1 Identifies Motifs Essential for Function. *Genetics* **213**, 1401–1414 (2019). doi: [10.1534/genetics.119.302601](https://doi.org/10.1534/genetics.119.302601); pmid: [31666291](https://pubmed.ncbi.nlm.nih.gov/31666291/)
51. T. A. Morrish *et al.*, DNA repair mediated by endonuclease-independent LINE-1 retrotransposition. *Nat. Genet.* **31**, 159–165 (2002). doi: [10.1038/ng898](https://doi.org/10.1038/ng898); pmid: [12006980](https://pubmed.ncbi.nlm.nih.gov/12006980/)
52. A. J. Doucet, J. E. Wilusz, T. Miyoshi, Y. Liu, J. V. Moran, A 3' Poly(A) Tract Is Required for LINE-1 Retrotransposition. *Mol. Cell* **60**, 728–741 (2015). doi: [10.1016/j.molcel.2015.10.012](https://doi.org/10.1016/j.molcel.2015.10.012); pmid: [26585388](https://pubmed.ncbi.nlm.nih.gov/26585388/)
53. L. Dai, M. S. Taylor, K. A. O'Donnell, J. D. Boeke, Poly(A) binding protein C1 is essential for efficient L1 retrotransposition and affects L1 RNP formation. *Mol. Cell. Biol.* **32**, 4323–4336 (2012). doi: [10.1128/MCB.06785-11](https://doi.org/10.1128/MCB.06785-11); pmid: [22907758](https://pubmed.ncbi.nlm.nih.gov/22907758/)
54. M. S. Taylor *et al.*, Affinity proteomics reveals human host factors implicated in discrete stages of LINE-1 retrotransposition. *Cell* **155**, 1034–1048 (2013). doi: [10.1016/j.cell.2013.10.021](https://doi.org/10.1016/j.cell.2013.10.021); pmid: [24267889](https://pubmed.ncbi.nlm.nih.gov/24267889/)
55. M. S. Taylor *et al.*, Dissection of affinity captured LINE-1 macromolecular complexes. *eLife* **7**, e30094 (2018). doi: [10.7554/eLife.30094](https://doi.org/10.7554/eLife.30094); pmid: [29309035](https://pubmed.ncbi.nlm.nih.gov/29309035/)
56. A. Luqman-Fatah *et al.*, The interferon stimulated gene-encoded protein HELZ2 inhibits human LINE-1 retrotransposition and LINE-1 RNA-mediated type I interferon induction. *Nat. Commun.* **14**, 203 (2023). doi: [10.1038/s41467-022-35757-6](https://doi.org/10.1038/s41467-022-35757-6); pmid: [36639706](https://pubmed.ncbi.nlm.nih.gov/36639706/)
57. J. B. Moldovan, J. V. Moran, The Zinc-Finger Antiviral Protein ZAP Inhibits LINE and Alu Retrotransposition. *PLOS Genet.* **11**, e1005121 (2015). doi: [10.1371/journal.pgen.1005121](https://doi.org/10.1371/journal.pgen.1005121); pmid: [25951186](https://pubmed.ncbi.nlm.nih.gov/25951186/)
58. J. L. Goodier, L. E. Cheung, H. H. Kazazian Jr., Mapping the LINE1 ORF1 protein interactome reveals associated inhibitors of human retrotransposition. *Nucleic Acids Res.* **41**, 7401–7419 (2013). doi: [10.1093/nar/gkt512](https://doi.org/10.1093/nar/gkt512); pmid: [23749060](https://pubmed.ncbi.nlm.nih.gov/23749060/)
59. J. Abramson *et al.*, Accurate structure prediction of biomolecular interactions with AlphaFold 3. *Nature* **630**, 493–500 (2024). doi: [10.1038/s41586-024-07487-w](https://doi.org/10.1038/s41586-024-07487-w); pmid: [38718835](https://pubmed.ncbi.nlm.nih.gov/38718835/)
60. A. González-Magaña, F. J. Blanco, Human PCNA Structure, Function and Interactions. *Biomolecules* **10**, 570 (2020). doi: [10.3390/biom10040570](https://doi.org/10.3390/biom10040570); pmid: [32276417](https://pubmed.ncbi.nlm.nih.gov/32276417/)
61. A. B. Sachs, R. W. Davis, The poly(A) binding protein is required for poly(A) shortening and 60S ribosomal subunit-dependent translation initiation. *Cell* **58**, 857–867 (1989). doi: [10.1016/0092-8674\(89\)90938-0](https://doi.org/10.1016/0092-8674(89)90938-0); pmid: [2673535](https://pubmed.ncbi.nlm.nih.gov/2673535/)
62. G. Caponigro, R. Parker, Multiple functions for the poly(A)-binding protein in mRNA decapping and deadenylation in yeast. *Genes Dev.* **9**, 2421–2432 (1995). doi: [10.1101/gad.9.19.2421](https://doi.org/10.1101/gad.9.19.2421); pmid: [7557393](https://pubmed.ncbi.nlm.nih.gov/7557393/)
63. J. M. Collier, N. K. Gray, M. P. Wickens, mRNA stabilization by poly(A) binding protein is independent of poly(A) and requires translation. *Genes Dev.* **12**, 3226–3235 (1998). doi: [10.1101/gad.12.20.3226](https://doi.org/10.1101/gad.12.20.3226); pmid: [9784497](https://pubmed.ncbi.nlm.nih.gov/9784497/)
64. A. C. Goldstrohm, M. Wickens, Multifunctional deadenylase complexes diversify mRNA control. *Nat. Rev. Mol. Cell Biol.* **9**, 337–344 (2008). doi: [10.1038/nrm2370](https://doi.org/10.1038/nrm2370); pmid: [18334997](https://pubmed.ncbi.nlm.nih.gov/18334997/)
65. L. Weill, E. Belloc, F.-A. Bava, R. Méndez, Translational control by changes in poly(A) tail length: Recycling mRNAs. *Nat. Struct. Mol. Biol.* **19**, 577–585 (2012). doi: [10.1038/nsmb.2311](https://doi.org/10.1038/nsmb.2311); pmid: [22664985](https://pubmed.ncbi.nlm.nih.gov/22664985/)
66. H. Yi *et al.*, PABP Cooperates with the CCR4-NOT Complex to Promote mRNA Deadenylation and Block Precoincis Decay. *Mol. Cell* **70**, 1081–1088.e5 (2018). doi: [10.1016/j.molcel.2018.05.009](https://doi.org/10.1016/j.molcel.2018.05.009); pmid: [29932901](https://pubmed.ncbi.nlm.nih.gov/29932901/)
67. M. W. Webster *et al.*, mRNA Deadenylation Is Coupled to Translation Rates by the Differential Activities of Ccr4-Not Nucleases. *Mol. Cell* **70**, 1089–1100.e8 (2018). doi: [10.1016/j.molcel.2018.05.033](https://doi.org/10.1016/j.molcel.2018.05.033); pmid: [29932902](https://pubmed.ncbi.nlm.nih.gov/29932902/)
68. A. L. Nicholson, A. E. Pasquinelli, Tales of Detailed Poly(A) Tails. *Trends Cell Biol.* **29**, 191–200 (2019). doi: [10.1016/j.tcb.2018.11.002](https://doi.org/10.1016/j.tcb.2018.11.002); pmid: [30503240](https://pubmed.ncbi.nlm.nih.gov/30503240/)
69. A. B. Sachs, R. W. Davis, R. D. Kornberg, A single domain of yeast poly(A)-binding protein is necessary and sufficient for RNA binding and cell viability. *Mol. Cell. Biol.* **7**, 3268–3276 (1987). doi: [10.1128/mcb.7.9.3268-3276.1987](https://doi.org/10.1128/mcb.7.9.3268-3276.1987); pmid: [3313012](https://pubmed.ncbi.nlm.nih.gov/3313012/)
70. U. Kühn, T. Pieler, Xenopus poly(A) binding protein: Functional domains in RNA binding and protein-protein interaction. *J. Mol. Biol.* **256**, 20–30 (1996). doi: [10.1006/jmbi.1996.0065](https://doi.org/10.1006/jmbi.1996.0065); pmid: [8609610](https://pubmed.ncbi.nlm.nih.gov/8609610/)
71. U. Kühn, E. Wahle, Structure and function of poly(A) binding proteins. *Biochim. Biophys. Acta* **1678**, 67–84 (2004). doi: [10.1016/j.bbexp.2004.03.008](https://doi.org/10.1016/j.bbexp.2004.03.008); pmid: [15157733](https://pubmed.ncbi.nlm.nih.gov/15157733/)
72. I. A. Eliseeva, D. N. Lyabin, L. P. Ovchinnikov, Poly(A)-binding proteins: Structure, domain organization, and activity regulation. *Biochemistry* **78**, 1377–1391 (2013). doi: [10.1134/S0006297913130014](https://doi.org/10.1134/S0006297913130014); pmid: [24490729](https://pubmed.ncbi.nlm.nih.gov/24490729/)
73. R. C. Deo, J. B. Bonanno, N. Sonenberg, S. K. Burley, Recognition of polyadenylate RNA by the poly(A)-binding protein. *Cell* **98**, 835–845 (1999). doi: [10.1016/S0092-8674\(00\)81517-2](https://doi.org/10.1016/S0092-8674(00)81517-2); pmid: [10499800](https://pubmed.ncbi.nlm.nih.gov/10499800/)
74. W. Wei *et al.*, Human L1 Retrotransposition: *cis* Preference versus *trans* Complementation. *Mol. Cell. Biol.* **21**, 1429–1439 (2001). doi: [10.1128/MCB.21.4.1429-1439.2001](https://doi.org/10.1128/MCB.21.4.1429-1439.2001); pmid: [11158327](https://pubmed.ncbi.nlm.nih.gov/11158327/)
75. J. D. Boeke, LINES and *Alus*—The polyA connection. *Nat. Genet.* **16**, 6–7 (1997). doi: [10.1038/ng0597-6](https://doi.org/10.1038/ng0597-6); pmid: [9140383](https://pubmed.ncbi.nlm.nih.gov/9140383/)
76. D. A. Mangus, M. C. Evans, A. Jacobson, Poly(A)-binding proteins: Multifunctional scaffolds for the post-transcriptional control of gene expression. *Genome Biol.* **4**, 223 (2003). doi: [10.1186/gb-2003-4-7-223](https://doi.org/10.1186/gb-2003-4-7-223); pmid: [12844354](https://pubmed.ncbi.nlm.nih.gov/12844354/)
77. R. Sawazaki *et al.*, Characterization of the multimeric structure of poly(A)-binding protein on a poly(A) tail. *Sci. Rep.* **8**, 1455 (2018). doi: [10.1038/s41598-018-19659-6](https://doi.org/10.1038/s41598-018-19659-6); pmid: [29362417](https://pubmed.ncbi.nlm.nih.gov/29362417/)
78. J. Park *et al.*, Short poly(A) tails are protected from deadenylation by the LARP1-PABP complex. *Nat. Struct. Mol. Biol.* **30**, 330–338 (2023). doi: [10.1038/s41594-023-00930-y](https://doi.org/10.1038/s41594-023-00930-y); pmid: [36849640](https://pubmed.ncbi.nlm.nih.gov/36849640/)
79. M. Dewannieux, T. Heidmann, Role of poly(A) tail length in Alu retrotransposition. *Genomics* **86**, 378–381 (2005). doi: [10.1016/j.ygeno.2005.05.009](https://doi.org/10.1016/j.ygeno.2005.05.009); pmid: [15993034](https://pubmed.ncbi.nlm.nih.gov/15993034/)
80. P. Mita *et al.*, LINE-1 protein localization and functional dynamics during the cell cycle. *eLife* **7**, e30058 (2018). doi: [10.7554/eLife.30058](https://doi.org/10.7554/eLife.30058); pmid: [29309036](https://pubmed.ncbi.nlm.nih.gov/29309036/)
81. D. A. Flasch *et al.*, Genome-wide *de novo* L1 Retrotransposition Connects Endonuclease Activity with Replication. *Cell* **177**, 837–851.e28 (2019). doi: [10.1016/j.cell.2019.02.050](https://doi.org/10.1016/j.cell.2019.02.050); pmid: [30955886](https://pubmed.ncbi.nlm.nih.gov/30955886/)
82. T. Sultana *et al.*, The Landscape of L1 Retrotransposons in the Human Genome Is Shaped by Pre-insertion Sequence Biases and Post-insertion Selection. *Mol. Cell* **74**, 555–570.e7 (2019). doi: [10.1016/j.molcel.2019.02.036](https://doi.org/10.1016/j.molcel.2019.02.036); pmid: [30956044](https://pubmed.ncbi.nlm.nih.gov/30956044/)
83. S. Trowitzsch, C. Bieniossek, Y. Nie, F. Garzoni, I. Berger, New baculovirus expression tools for recombinant protein complex production. *J. Struct. Biol.* **172**, 45–54 (2010). doi: [10.1016/j.jsb.2010.02.010](https://doi.org/10.1016/j.jsb.2010.02.010); pmid: [20178849](https://pubmed.ncbi.nlm.nih.gov/20178849/)
84. Y. He, J. Fang, D. J. Taatjes, E. Nogales, Structural visualization of key steps in human transcription initiation. *Nature* **495**, 481–486 (2013). doi: [10.1038/nature11991](https://doi.org/10.1038/nature11991); pmid: [23446344](https://pubmed.ncbi.nlm.nih.gov/23446344/)
85. M. Bokori-Brown *et al.*, Cryo-EM structure of lysenin pore elucidates membrane insertion by an aerolysin family protein. *Nat. Commun.* **7**, 11293 (2016). doi: [10.1038/ncomms11293](https://doi.org/10.1038/ncomms11293); pmid: [27048994](https://pubmed.ncbi.nlm.nih.gov/27048994/)
86. A. Boland *et al.*, Cryo-EM structure of a metazoan separate-securin complex at near-atomic resolution. *Nat. Struct. Mol. Biol.* **24**, 414–418 (2017). doi: [10.1038/nsmb.3386](https://doi.org/10.1038/nsmb.3386); pmid: [28263324](https://pubmed.ncbi.nlm.nih.gov/28263324/)

87. A. Rohou, N. Grigorieff, CTFIND4: Fast and accurate defocus estimation from electron micrographs. *J. Struct. Biol.* **192**, 216–221 (2015). doi: [10.1016/j.jsb.2015.08.008](https://doi.org/10.1016/j.jsb.2015.08.008); pmid: [26278980](https://pubmed.ncbi.nlm.nih.gov/26278980/)
88. T. Bepko *et al.*, Positive-unlabeled convolutional neural networks for particle picking in cryo-electron micrographs. *Nat. Methods* **16**, 1153–1160 (2019). doi: [10.1038/s41592-019-0575-8](https://doi.org/10.1038/s41592-019-0575-8); pmid: [31591578](https://pubmed.ncbi.nlm.nih.gov/31591578/)
89. J. Zivanov, T. Nakane, S. H. W. Scheres, Estimation of high-order aberrations and anisotropic magnification from cryo-EM data sets in RELION-3.1. *IUCr* **7**, 253–267 (2020). doi: [10.1107/S2052252520000081](https://doi.org/10.1107/S2052252520000081); pmid: [32148853](https://pubmed.ncbi.nlm.nih.gov/32148853/)
90. J. Zivanov, T. Nakane, S. H. W. Scheres, A Bayesian approach to beam-induced motion correction in cryo-EM single-particle analysis. *IUCr* **6**, 5–17 (2019). doi: [10.1107/S205225251801463X](https://doi.org/10.1107/S205225251801463X); pmid: [30713699](https://pubmed.ncbi.nlm.nih.gov/30713699/)
91. A. Punjani, J. L. Rubinstein, D. J. Fleet, M. A. Brubaker, cryoSPARC: Algorithms for rapid unsupervised cryo-EM structure determination. *Nat. Methods* **14**, 290–296 (2017). doi: [10.1038/nmeth.4169](https://doi.org/10.1038/nmeth.4169); pmid: [28165473](https://pubmed.ncbi.nlm.nih.gov/28165473/)
92. A. Punjani, H. Zhang, D. J. Fleet, Non-uniform refinement: Adaptive regularization improves single-particle cryo-EM reconstruction. *Nat. Methods* **17**, 1214–1221 (2020). doi: [10.1038/s41592-020-00990-8](https://doi.org/10.1038/s41592-020-00990-8); pmid: [33257830](https://pubmed.ncbi.nlm.nih.gov/33257830/)
93. D. Asarnow, E. Palovcak, Y. Cheng, asarnow/pyem: UCSF pyem v0.5. *Zenodo* (2019). doi: [10.5281/zenodo.3576630](https://doi.org/10.5281/zenodo.3576630)
94. S. Chaaban, sami-chaaban/starparser: v1.38. *Zenodo* (2022). doi: [10.5281/zenodo.6792794](https://doi.org/10.5281/zenodo.6792794)
95. T. Nakane, D. Kimanius, E. Lindahl, S. H. Scheres, Characterisation of molecular motions in cryo-EM single-particle data by multi-body refinement in RELION. *eLife* **7**, e36861 (2018). doi: [10.7554/eLife.36861](https://doi.org/10.7554/eLife.36861); pmid: [29856314](https://pubmed.ncbi.nlm.nih.gov/29856314/)
96. T. Nakane, S. H. W. Scheres, Multi-body Refinement of Cryo-EM Images in RELION. *Methods Mol. Biol.* **2215**, 145–160 (2021). doi: [10.1007/978-1-0716-0966-8_7](https://doi.org/10.1007/978-1-0716-0966-8_7); pmid: [33368003](https://pubmed.ncbi.nlm.nih.gov/33368003/)
97. Y. Z. Tan *et al.*, Addressing preferred specimen orientation in single-particle cryo-EM through tilting. *Nat. Methods* **14**, 793–796 (2017). doi: [10.1038/nmeth.4347](https://doi.org/10.1038/nmeth.4347); pmid: [28671674](https://pubmed.ncbi.nlm.nih.gov/28671674/)
98. J. Jumper *et al.*, Highly accurate protein structure prediction with AlphaFold. *Nature* **596**, 583–589 (2021). doi: [10.1038/s41586-021-03819-2](https://doi.org/10.1038/s41586-021-03819-2); pmid: [34265844](https://pubmed.ncbi.nlm.nih.gov/34265844/)
99. T. I. Croll, ISOLDE: A physically realistic environment for model building into low-resolution electron-density maps. *Acta Crystallogr. D Struct. Biol.* **74**, 519–530 (2018). doi: [10.1107/S2059798318002425](https://doi.org/10.1107/S2059798318002425); pmid: [29872003](https://pubmed.ncbi.nlm.nih.gov/29872003/)
100. A. Casañal, B. Lohkamp, P. Emsley, Current developments in Coot for macromolecular model building of Electron Cryo-microscopy and Crystallographic Data. *Protein Sci.* **29**, 1069–1078 (2020). doi: [10.1002/pro.3791](https://doi.org/10.1002/pro.3791); pmid: [31730249](https://pubmed.ncbi.nlm.nih.gov/31730249/)
101. G. N. Murshudov *et al.*, REFMAC5 for the refinement of macromolecular crystal structures. *Acta Crystallogr. D Biol. Crystallogr.* **67**, 355–367 (2011). doi: [10.1107/S0907444911001314](https://doi.org/10.1107/S0907444911001314); pmid: [21460544](https://pubmed.ncbi.nlm.nih.gov/21460544/)
102. D. Liebschner *et al.*, Macromolecular structure determination using X-rays, neutrons and electrons: Recent developments in Phenix. *Acta Crystallogr. D Biol. Crystallogr.* **75**, 861–877 (2019). doi: [10.1107/S2059798319011471](https://doi.org/10.1107/S2059798319011471); pmid: [31588918](https://pubmed.ncbi.nlm.nih.gov/31588918/)
103. K. Yamashita, C. M. Palmer, T. Burnley, G. N. Murshudov, Cryo-EM single-particle structure refinement and map calculation using Servalcat. *Acta Crystallogr. D Struct. Biol.* **77**, 1282–1291 (2021). doi: [10.1107/S2059798321009475](https://doi.org/10.1107/S2059798321009475); pmid: [34605431](https://pubmed.ncbi.nlm.nih.gov/34605431/)
104. R. A. Nicholls, F. Long, G. N. Murshudov, Low-resolution refinement tools in REFMAC5. *Acta Crystallogr. D Biol. Crystallogr.* **68**, 404–417 (2012). doi: [10.1107/S090744491105606X](https://doi.org/10.1107/S090744491105606X); pmid: [22505260](https://pubmed.ncbi.nlm.nih.gov/22505260/)
105. A. Brown *et al.*, Tools for macromolecular model building and refinement into electron cryo-microscopy reconstructions. *Acta Crystallogr. D Biol. Crystallogr.* **71**, 136–153 (2015). doi: [10.1107/S1399004714021683](https://doi.org/10.1107/S1399004714021683); pmid: [25615868](https://pubmed.ncbi.nlm.nih.gov/25615868/)
106. E. C. Meng *et al.*, UCSF ChimeraX: Tools for structure building and analysis. *Protein Sci.* **32**, e4792 (2023). doi: [10.1002/pro.4792](https://doi.org/10.1002/pro.4792); pmid: [37774136](https://pubmed.ncbi.nlm.nih.gov/37774136/)
107. The UniProt Consortium, UniProt: The Universal Protein Knowledgebase in 2023. *Nucleic Acids Res.* **51**, D523–D531 (2023). doi: [10.1093/nar/gkac1052](https://doi.org/10.1093/nar/gkac1052); pmid: [36408920](https://pubmed.ncbi.nlm.nih.gov/36408920/)
108. S. Boissinot, A. Sookdeo, The Evolution of LINE-1 in Vertebrates. *Genome Biol. Evol.* **8**, 3485–3507 (2016). doi: [10.1093/gbe/evw247](https://doi.org/10.1093/gbe/evw247); pmid: [28175298](https://pubmed.ncbi.nlm.nih.gov/28175298/)
109. F. Sievers *et al.*, Fast, scalable generation of high-quality protein multiple sequence alignments using Clustal Omega. *Mol. Syst. Biol.* **7**, 539 (2011). doi: [10.1038/msb.2011.75](https://doi.org/10.1038/msb.2011.75); pmid: [21988835](https://pubmed.ncbi.nlm.nih.gov/21988835/)
110. G. Ghanim, H. Hu, J. Boulanger, T. H. D. Nguyen, Structural mechanism of LINE-1 target-primed reverse transcription. *Zenodo* (2025). doi: [10.5281/zenodo.14840913](https://doi.org/10.5281/zenodo.14840913)

ACKNOWLEDGMENTS

We thank D. Rio, D. Black, M. Wilkinson, J. Roske, and J. Stowell for valuable discussions; D. Rio for the kind gift of a codon-optimized ORF2p construct; the Laboratory of Molecular Biology (LMB) EM facility staff and B. Ahsan for access to and support for EM sample preparation and data collection; J. Grimmert, T. Darling, and I. Clayton for maintaining the scientific computing resources; the LMB Light Microscopy facility, especially T. P. de Azevedo, for training and support with light microscopy experiments; ChatGPT for the initial (albeit bug-ridden) python code to map activity onto the PDB file; H. Yan for providing graphene oxide-coated grids for testing; P. Emsley and L. Catapano for help with Coot; J. Schwab, K. Naydenova, and S. Chaaban for data processing advice; the Löwe, Passmore, and Scheres laboratories for sharing reagents, equipment, and technical advice; and D. Rio, R. Hegde, P. Lehner, and Z. Sekne for critical reading of the manuscript. **Funding:** This study was supported by a Jane Coffin Childs Postdoctoral Fellowship (G.E.G.), UK Research and Innovation (UKRI)—Medical

Research Council grant MC_UP_1201/19 (T.H.D.N.), and an EMBO Young Investigator Program Award (T.H.D.N.). **Author contributions:** G.E.G. initiated the project. G.E.G. purified samples, performed biochemical experiments, prepared EM grids, and collected and analyzed EM data. G.E.G. performed model building and refinement. H.H. assisted G.E.G. with initial cryo-EM data collection and biochemical experiments. T.H.D.N. performed light microscopy experiments. J.B. performed light microscopy data analysis. G.E.G. and T.H.D.N. analyzed the biochemical data and the structures. G.E.G. wrote the first draft. G.E.G. and T.H.D.N. prepared illustrations. G.E.G. and T.H.D.N. prepared the final version of the manuscript. **Competing interests:** The authors declare that they have no competing interests. **Data and materials availability:** The cryo-EM maps have been deposited in the Electron Microscopy Data Bank under the following accession codes: EMD-52070 for the consensus TPRT complex, EMD-52072 for the open fingers state, EMD-52071 for the closed fingers state, and EMD-52073 for the EN domain-resolved TPRT complex. The coordinates for the atomic models have been deposited in the Protein Data Bank under the following accession codes: 9HDO for the consensus TPRT complex, 9HDQ for the open fingers state, 9HDP for the closed fingers state, and 9HDR for the EN-resolved TPRT complex. The raw cryo-EM micrographs have been deposited in EMPIAR with accession code EMPIAR-12450. AlphaFold3 predictions have been deposited in ModelArchive with accession codes ma-w0esd (ORF2p-PCNA-target DNA) and ma-lhurr (ORF2p-PABPC1-RRM1-2-RNA). The scripts used in this manuscript are available at Zenodo ([110](https://doi.org/110)). Materials are available from T.H.D.N. under a material transfer agreement with the MRC—Laboratory of Molecular Biology. **License information:** Copyright © 2025 the authors, some rights reserved; exclusive licensee American Association for the Advancement of Science. No claim to original US government works. <https://www.science.org/about/science-licenses-journal-article-reuse>. This research was funded in whole or in part by UKRI (MC_UP_1201/19), a cOAlition S organization. The author will make the Author Accepted Manuscript (AAM) version available under a CC BY public copyright license.

SUPPLEMENTARY MATERIALS

science.org/doi/10.1126/science.ads8412

Supplementary Text
Figs. S1 to S13
Tables S1 and S2
References ([111–114](#))
MDAR Reproducibility Checklist
Data S1
Movies S1 to S3

Submitted 30 August 2024; accepted 11 February 2025

Published online 6 March 2025

[10.1126/science.ads8412](https://doi.org/10.1126/science.ads8412)